AGU100 ADVANCING EARTH AND SPACE SCIENCE

JGR

Journal of Geophysical Research: Solid Earth

RESEARCH ARTICLE

10.1029/2018JB016558

Global Analysis of Experimental Data on the Rheology of Olivine Aggregates

Chhavi Jain[1], **Jun Korenaga**[1], **and Shun-ichiro Karato**[1]

[1] Department of Geology and Geophysics, Yale University, New Haven, CT, USA

Key Points:

- Published experimental data are analyzed simultaneously for composite rheology
- Treatment of interrun biases in Markov chain Monte Carlo inversion is made more efficient
- Candidate rheological models are proposed for geodynamical applications

Supporting Information:

- Supporting Information S1

Correspondence to:

C. Jain,
chhavi.jain@yale.edu

Citation:

Jain, C., Korenaga, J., & Karato, S. (2019). Global analysis of experimental data on the rheology of olivine aggregates. *Journal of Geophysical Research: Solid Earth*, *124*, 310–334. https://doi.org/10.1029/2018JB016558

Received 15 AUG 2018
Accepted 11 DEC 2018
Accepted article online 13 DEC 2018
Published online 22 JAN 2019

Abstract Following the reanalysis of individual experimental runs of some widely cited studies (Jain et al., 2018, https://doi.org/10.1002/2017JB014847), we revisit the global data analysis of Korenaga and Karato (2008, https://doi.org/10.1029/2007JB005100) with a significantly improved version of their Markov chain Monte Carlo inversion. Their algorithm, previously corrected by Mullet et al. (2015) to minimize potential parameter bias, is further modified here to estimate more efficiently interrun biases in global data sets. Using the refined Markov chain Monte Carlo inversion technique, we simultaneously analyze experimental data on the deformation of olivine aggregates compiled from different studies. Realistic composite rheological models, including both diffusion and dislocation creep, are adopted, and the role of dislocation-accommodated grain boundary sliding is also investigated. Furthermore, the influence of interrun biases on inversion results is studied using experimental and synthetic data. Our analysis shows that existing data can tightly constrain the grain-size exponent for diffusion creep at ~2, which is different from the value commonly assumed ($p = 3$). Different data sets and model assumptions, however, yield nonoverlapping estimates on other flow-law parameters, and the flow-law parameters for grain boundary sliding are poorly resolved in most cases. We thus provide a few plausible candidate flow-law models for olivine rheology to facilitate future geodynamic modeling. The availability of more data that explore a wider range of experimental conditions, especially higher pressures, is essential to improve our understanding of upper mantle rheology.

1. Introduction

The rheology of the upper mantle is often modeled using the flow-law parameters of olivine aggregates (e.g., Alisic et al., 2012; Garel et al., 2014; Hedjazian et al., 2017; Kohlstedt et al., 1995; Solomatov, 1995), because olivine is the most abundant and usually the weakest phase of the upper mantle (e.g., Karato & Wu, 1993). However, estimates on these flow-law parameters, derived from the inversion of experimental deformation data, are not unique. For example, the flow laws for diffusion and dislocation creep suggested by Hirth and Kohlstedt (2003) and Korenaga and Karato (2008) differ significantly. Also, our recent reanalysis of some experimental studies, such as Karato et al. (1986) and Mei and Kohlstedt (2000a, 2000b), on olivine rheology revealed that the range of conditions explored in a single experimental run was too narrow to accurately constrain flow-law parameters for these two creep regimes (Jain et al., 2018). It was suggested that simultaneously inverting data from multiple experimental runs and even different studies ("global inversion") could yield more reliable results.

A potential problem with global inversion is the existence of interrun bias (Korenaga & Karato, 2008). We define interrun bias as a systematic difference in strain rates observed between different experimental runs after being normalized to the same experimental conditions. It could arise due to a number of reasons, for example, change in instrument calibration between consecutive runs or the unaccounted loss or gain of water during an experiment. It can also be caused by variation in silica activity, which is fixed by adding a small amount of enstatite in some studies (e.g., Hirth & Kohlstedt, 1995; Mei & Kohlstedt, 2000a, 2000b) but not in others (e.g., Karato et al., 1986). The presence of a trace amount of melt in a sample or difference in sample composition could also be factors. For example, the synthetic samples of Fo_{90} olivine prepared by Faul and Jackson (2007) using a new sol-gel technique were found to be systematically stronger than the samples of previous studies, such as Karato et al. (1986) and Mei and Kohlstedt (2000a, 2000b), possibly because of the complete absence of melt in the sol-gel samples. The difference could also be caused by the different amount of impurities in the sol-gel samples and the other samples. Global inversion must take such interrun biases into account.

Korenaga and Karato (2008) conducted global inversion for olivine rheology using a Markov chain Monte Carlo (MCMC) inversion technique, and they treated interrun bias factors as additional model parameters to be estimated by MCMC sampling. However, this made the parameter space being sampled considerably more multidimensional. Moreover, in the absence of any theoretical or experimental bounds on these biases, wide a priori bounds needed to be assumed for these parameters. To improve the efficiency of the MCMC inversion scheme, we modify their algorithm to estimate these bias factors separately from MCMC sampling.

In this study, we compile published experimental data on the deformation of olivine aggregates and reanalyze them collectively for diffusion and dislocation creep (i.e., composite flow law) using our modified MCMC algorithm. Some studies have suggested that dislocation-accommodated grain boundary sliding (GBS) may also be a rate-limiting mechanism (e.g., Hansen et al., 2011; Hirth & Kohlstedt, 2015). We thus test the importance of this mechanism as well. Our goal is to obtain a set of flow-law parameters for olivine aggregates that fit most of the available experimental data. We consider data from a number of experimental studies for our reanalysis and find that different data compilations, or different model assumptions, can yield distinct constraints on flow-law parameters. As such, we summarize our reanalysis by providing some candidate rheological models for olivine so that the current uncertainty of olivine rheology can easily be reflected in geodynamical studies.

Important differences exist between our global data analyses and those conducted by Korenaga and Karato (2008; hereinafter referred to as KK08). The inversion scheme used by KK08 was recently found to potentially favor larger values of flow-law parameters over smaller ones, even if both values yielded the same mismatch with observed data ("parameter bias"), and this bias might have influenced their results (Mullet et al., 2015). Our MCMC inversion code, adopted from Mullet et al. (2015), is corrected for this bias and modified to better constrain the scaling coefficients. We have made further improvements to the code to minimize the influence of interrun biases. Furthermore, KK08 simultaneously analyzed all data from four experimental studies. However, our recent analysis of individual experimental runs from these studies (Jain et al., 2018) identified some erroneous data, which need to be excluded. Also, our data compilation includes additional data sets from Hansen et al. (2011) and Ohuchi et al. (2015). Because of these differences, most of flow-law parameters estimated in this study differ from those reported by KK08. Because of the aforementioned improvements made to the MCMC inversion scheme and data selection, our estimates are likely to be more reliable.

The structure of this paper is as follows. First, we describe our composite rheological model and our modified MCMC algorithm. Then, we will use this algorithm to assess how different global data sets constrain the flow-law parameters of diffusion and dislocation creep. Dry and wet data will be analyzed separately. The significance of GBS under both conditions will be discussed by comparing results for two composite models, one that includes GBS and one that does not. The influence of interrun bias on our inversion results will also be investigated. We will conclude with an assessment of the geophysical relevance of our results and some suggestions for how to improve our understanding of the flow laws.

2. Mathematical Framework

2.1. Composite Rheological Model

The constitutive equations that govern the steady state deformation of olivine aggregates in the diffusion, dislocation, and GBS creep regimes are (e.g., Karato, 2008)

$$\dot{\epsilon}_{\mathrm{diff,dry}} = \dot{\epsilon_1} = A_1 d^{-p_1} \sigma \exp\left(-\frac{E_1 + PV_1}{RT}\right), \tag{1}$$

$$\dot{\epsilon}_{\mathrm{diff,wet}} = \dot{\epsilon_2} = A_2 d^{-p_2} C_w^{r_2} \sigma \exp\left(-\frac{E_2 + PV_2}{RT}\right), \tag{2}$$

$$\dot{\epsilon}_{\mathrm{disl,dry}} = \dot{\epsilon_3} = A_3 \sigma^{n_3} \exp\left(-\frac{E_3 + PV_3}{RT}\right), \tag{3}$$

$$\dot{\epsilon}_{\mathrm{disl,wet}} = \dot{\epsilon_4} = A_4 \sigma^{n_4} C_w^{r_4} \exp\left(-\frac{E_4 + PV_4}{RT}\right), \tag{4}$$

$$\dot{\epsilon}_{\mathrm{gbs,dry}} = \dot{\epsilon_5} = A_5 d^{-p_5} \sigma^{n_5} \exp\left(-\frac{E_5 + PV_5}{RT}\right), \tag{5}$$

$$\dot{\epsilon}_{\mathrm{gbs,wet}} = \dot{\epsilon_6} = A_6 d^{-p_6} \sigma^{n_6} C_w^{r_6} \exp\left(-\frac{E_6 + PV_6}{RT}\right). \tag{6}$$

Here strain rate for each creep mechanism under dry or wet conditions is denoted by $\dot{\epsilon}_i$ (in s^{-1}), for example, $\dot{\epsilon}_1$ denotes diffusion creep under dry conditions. It is a function of the average grain size, d (in microns); the deviatoric stress, σ (in MPa); the pressure, P (in Pa); and the absolute temperature, T (in K), and R is the gas constant. Under wet conditions, strain rate also depends on the water content, C_w (in ppm H/Si). The scaling coefficient for the ith flow law, A_i, is in $s^{-1}MPa^{-n_i}\mu m^{p_i}$ under dry conditions. We write the wet flow laws in terms of water content rather than water fugacity because we consider a model where water content is fixed, that is, a closed system behavior.

In equations (1)–(6), p_i, n_i, and r_i are the grain-size, stress, and water-content exponents, respectively, for the ith flow law. In the diffusion creep regime, strain rate is a nonlinear function of grain size but is assumed to depend linearly on stress (i.e., $n_1 = n_2 = 1$). In the dislocation creep regime, deformation is independent of grain size (i.e., $p_3 = p_4 = 0$) but varies nonlinearly with stress. Strain rate is a function of both grain size and stress in the GBS regime. The dependence of strain rate on temperature and pressure in all six flow laws is characterized by the activation energy, E_i, and the activation volume, V_i, respectively.

Experimental conditions usually lie close to the boundary between the diffusion and the dislocation creep regimes (e.g., Karato, 2010; Karato & Wu, 1993), and these two creep mechanisms most likely operate in parallel to produce the observed deformation. It is, therefore, more appropriate to model observed strain rates by composite rheology, that is, as a sum of the strain rates predicted by the flow laws for diffusion and dislocation creep. Because GBS may also be important under similar conditions, the composite rheological model may include this mechanism as well. We do not account for low-temperature plasticity because its contribution to the total deformation is negligible under the range of experimental conditions considered here (section S1). We assume that the observed strain rates ($\dot{\epsilon}_{obs}$) under nominally anhydrous ("dry") conditions can be entirely modeled by dry flow laws and those under hydrous ("wet") conditions entirely by wet flow laws. We will discuss the validity of this assumption for modeling wet data in section 5. The composite flow law is, therefore, represented by the following equation:

$$\dot{\epsilon}_{obs} = \sum_i \dot{\epsilon}_i \left(\{q_k\}; \{s_l\}\right), \tag{7}$$

where i can represent a combination of two or more flow laws among equations (1), (3), and (5) under dry conditions and equations (2), (4), and (6) under wet conditions and $\dot{\epsilon}_i \left(\{q_k\}; \{s_l\}\right)$ are the corresponding flow-law predictions using the set of model parameters denoted by $\{q_k\}$ at the experimental conditions represented by $\{s_l\}$. Individually, each of the constitutive equations (1)–(6) may be linearized by taking the logarithm of the strain rates, but the same cannot be done for a composite flow law (equation (7)). To fit the composite flow law to data, therefore, we require a nonlinear inversion technique. The MCMC algorithm of KK08 is designed to tackle such nonlinear inverse problems. Note that equation (7) assumes that observations do not contain any interrun biases.

The quantities P, T, $\dot{\epsilon}$, σ, d, and C_w in equations (1)–(6) constitute input parameters for our inverse problem. Of these, P, T, $\dot{\epsilon}$, and σ are measured during an experiment whereas C_w is often calculated at given T and P conditions assuming water saturation (Kohlstedt et al., 1996; Zhao et al., 2004). The sample grain size is usually measured at the beginning and the end of an experiment, and the intermediate grain sizes are interpolated assuming a grain growth equation (Karato, 1989). Using these input parameters, a total of up to 29 flow-law parameters can be estimated: 6 A_i's, 6 E_i's, 6 V_i's, 4 n_i's, 4 p_i's, and 3 r_i's.

2.2. MCMC Inversion

The MCMC inversion technique is based on an iterative procedure. In each iteration, a random value of a flow-law parameter is sampled from a given a priori range and substituted into the model equation (7). The misfit between the observed strain rates and those predicted by the trial model is evaluated. A trial model with a smaller misfit has a higher likelihood of explaining data. A trial model is then accepted or rejected based on a rejection scheme, and the algorithm moves to the next iteration. When the number of model parameters increases, a larger number of iterations are usually required to explore the entire model space. The MCMC algorithm designed by KK08 employs the Gibbs sampling to identify part of the model space that is likely to produce smaller misfits.

All of the experimental variables are associated with some uncertainties, and the MCMC inversion scheme can take these data uncertainties into account. However, a source of error that is more difficult to account for is interrun bias. Interrun bias represents systematic differences between strain rates of different experimental runs compared at identical conditions. If each experimental run is inverted separately, these systematic differences will manifest as discrepant values of the scaling factors A_i. When data from different experimental runs or different studies are simultaneously analyzed in a global inversion, these systematic errors need to be incorporated in the model. As strain rates for a group of runs can exhibit the same systematic deviation from those for another group of runs, interrun bias will denote systematic errors between data groups, each of which includes one or more individual runs. An interrun bias factor, X_m, corresponding to the mth data group is, therefore, introduced in our composite rheological model (equation (7)) as follows:

$$\dot{\epsilon}_{\text{obs}} = \left(\sum_i \dot{\epsilon}_i \left(\{q_k\}; \{s_l\} \right) \right) \cdot \exp(X_m). \tag{8}$$

The value of X_m is assumed to be constant over all data in the mth group but may differ between different groups. The interrun bias factor is expressed in an exponential term here so that when strain rates from different data groups are compared at the same conditions in the logarithmic space, they will differ from each other by X_m. Equation (8) is the model that we will fit to experimental data in this study.

KK08 estimated X_m using MCMC sampling. Their definition of the model misfit or cost function, represented by χ^2, therefore, included X_m, so that minimization of the cost function required MCMC sampling to search for optimal values of flow-law parameters as well as X_m. Their cost function was later modified by Mullet et al. (2015) to avoid potential parameter bias. The modified method minimizes the following cost function:

$$\chi^2_{\text{M}} \left(\{q_k\} \right) = \sum_{m=1}^{M} \left(\sum_{a=1}^{N_m} \frac{\left[\log \dot{\epsilon}_{\text{obs},a} - \log \left(\sum_i \dot{\epsilon}_i \left(\{q_k\}; \{s_l^a\} \right) \right) - X_m \right]^2}{\text{rvar}(\dot{\epsilon}_a)} \right). \tag{9}$$

This cost function, χ^2_{M}, is based on the difference between observed and predicted strain rates, measured in the logarithmic space. The predicted strain rate at each data point is evaluated using our composite rheological model (equation (8)) and corrected for interrun bias X_m, which is constant for each of N_m data points within the mth group. The total number of data groups is denoted by M. The squared difference is normalized by the relative variance of the observed strain rate, $\text{rvar}(\dot{\epsilon})$, where $\text{rvar}(\dot{\epsilon}) = \text{var}(\dot{\epsilon})/\dot{\epsilon}^2$, to account for the uncertainty of strain rate.

As explained in section 1, estimating a set of X_m values using MCMC sampling greatly expands our model space, leading to a substantial increase in the number of iterations to reach convergence. To decouple the estimation of X_m from MCMC sampling and improve its efficiency, we introduce some further modifications to the algorithm of Mullet et al. (2015) as described in the next section.

2.3. New Cost Function With Strain Rate Gradients

In the new MCMC scheme, instead of computing misfit by comparing the observed and predicted strain rates at each data point, we compare the gradients of strain rates, still in the logarithmic space. Difference in gradients, $\Delta^m_{a,b}$, is evaluated for each pair of data points, a and b, within the mth data group, as follows:

$$\Delta^m_{a,b} = \left[\log \dot{\epsilon}_{\text{obs},b} - \log \dot{\epsilon}_{\text{obs},a} \right] - \left[\log \left(\sum_i \dot{\epsilon}_i \left(\{q_k\}; \{s_l^b\} \right) \right) - \log \left(\sum_i \dot{\epsilon}_i \left(\{q_k\}; \{s_l^a\} \right) \right) \right]. \tag{10}$$

Here the expression in the first pair of brackets represents the observed gradient between the two data points, and that in the second pair represents the predicted gradient between them. Predicted strain rates are computed using our model equation (8), but because X_m in equation (8) is constant for all data belonging to the same group, it does not appear in equation (10). Using this gradient misfit, we define a new cost function, χ^2_{J}, as

$$\chi^2_{\text{J}} \left(\{q_k\} \right) = \sum_{m=1}^{M} \left(\sum_{a=1}^{N_m-1} \sum_{b=a+1}^{N_m} \frac{\left(\Delta^m_{a,b} \right)^2}{\text{rvar}(\dot{\epsilon}_a) + \text{rvar}(\dot{\epsilon}_b)} \right), \tag{11}$$

which will be minimized by MCMC sampling. Similar to χ^2_{M}, this cost function explicitly considers only the uncertainty of strain rates. Errors in other state variables are implicitly incorporated in our inversion scheme by periodically randomizing all data within their reported uncertainties (Mullet et al., 2015).

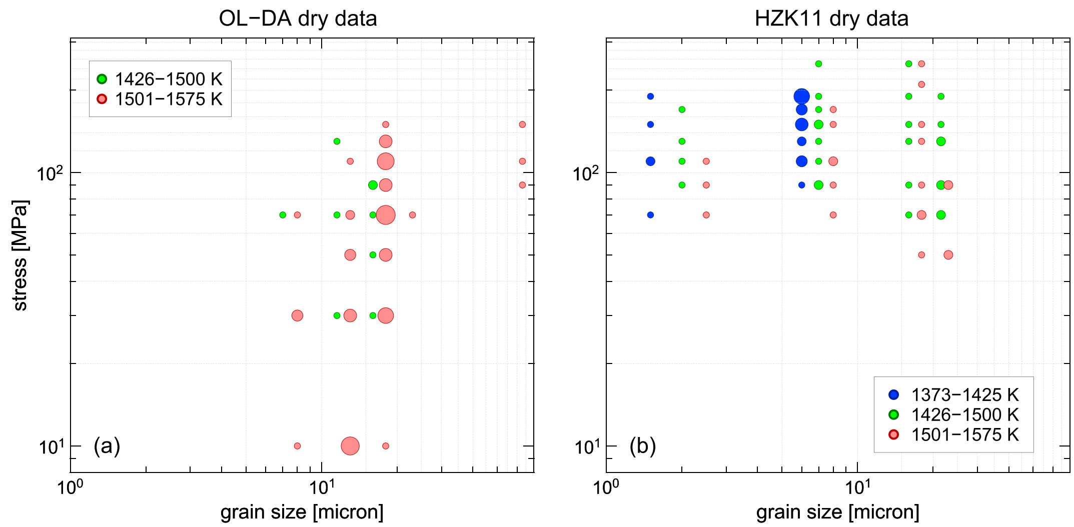

Figure 1. Range of experimental conditions explored by (a) three studies: KPF86, HK95, and MK00, and (b) HZK11 all under dry conditions. A three-dimensional mesh of grain sizes, stresses, and temperatures was created, with lower bounds of 0-μm grain size, 0-MPa stress, and 1,425-K temperature, and respective bin widths of 5 μm, 20 MPa, and 75 K. Experimental data are binned by this mesh. Gray lines mark the two-dimensional mesh in grain size and stress. Each circle represents the experimental observations within the grain size and stress bins. The color of the circle represents the temperature bin. The area of the circle is proportional to the bin count.

In the inversion algorithm of Mullet et al. (2015), the scaling coefficients A_i are evaluated in each iteration using the conjugate gradient method. We modify their conjugate gradient scheme to accommodate our new cost function and to link the estimation of A_i with that of X_m (Appendix A). The benchmark test of the new formulation is given in section S2. A sequence of all MCMC iterations is resampled, typically at every few hundred iterations, to obtain an ensemble of statistically independent models. The a posteriori probability distribution of each parameter so obtained can then be used to compute various statistical estimators, such as the mean and standard deviation. Because the original cost function of equation (9) is a more direct estimator of the model misfit, the normalized χ^2_{M}, that is, χ^2_{M}/N, where N is the total number of data points, is also computed.

The a posteriori probability distribution may not always be Gaussian; consequently, the mean model may not be a good fit to data. When summarizing our results, therefore, we only consider those MCMC outputs for which the normalized χ^2_{M} is greater than its minimum by at most a small percentage (usually 1–10%). The mean and standard deviation for each parameter are estimated from this truncated probability distribution. Consequently, the reported mean values of flow-law parameters and corresponding χ^2_{M}/N values may not always coincide with the peak in their respective a posteriori probability distributions. However, the mean model calculated this way usually coincides with the median and fits data reasonably well.

We note that the definition of χ^2_{M} or χ^2_{J} implicitly assumes that error in the logarithm of strain rate is normally distributed although it is more likely that error in strain rate, and not its logarithm, has a Gaussian distribution. To remove X_m from the definition of misfit, we must compare strain rates in the logarithmic space. As shown in Appendix B, for up to 10 % uncertainty in strain rate, the distribution of error in the logarithm of strain rate can be approximated by a normal distribution.

3. Reanalysis of Dry Experimental Data

In this section, we revisit experimental data on olivine rheology under dry conditions reported by Karato et al. (1986; hereinafter referred to as KPF86), Hirth and Kohlstedt (1995; HK95), Mei and Kohlstedt (2000a, 2000b; MK00), and Hansen et al. (2011; HZK11). We construct two global data sets, denoted as OL-DA and OL-DB (where the "D" stands for dry olivine rheology and "A" and "B" are the two different data sets), from them. OL-DA contains all dry data from the first three studies, spanning over a temperature range of 1,473–1,573 K, differential stresses of ∼6–150 MPa, and grain sizes of ∼7–60 μm (Figure 1a). OL-DB includes the experiments of HZK11 as well, which were conducted on fine-grained olivine aggregates under lower temperatures and higher stresses (Figure 1b). OL-DB, therefore, encompasses a wider range of experimental conditions. The

Table 1
Summary of Data Uncertainties

Data source	δT	δP	$\delta\sigma$	$\delta\dot{\epsilon}$	δd	δC_{OH}
Karato et al. (1986)[a]	10 K	5 MPa	2 MPa	1%	10%	20%
Hirth and Kohlstedt (1995)[a]	2 K	4 MPa	2 MPa	5%	10%	—[b]
Mei & Kohlstedt, (2000a, 2000b)[a]	2 K	4 MPa	2 MPa	5%	10–30%	20%
Jung et al. (2006)[a]	10 K	10 %	15 %	9–23%	10%	20%
Hansen et al. (2011)	2 K	1 MPa	1 MPa	10^{-6} s^{-1}[c]	10%[d]	—[b]
Ohuchi et al. (2015)	50 K	200 MPa	10–20%[e]	10%	10%	2–35%

[a]Taken from Korenaga and Karato (2008). Details are provided in their study. [b]All data are from dry experiments. [c]Estimate obtained from pers. comm. with L. Hansen in 2017. However, in some cases, this amounted to >80% uncertainty in strain rate, which is higher than that observed in older studies that used a similar apparatus under similar conditions (e.g., Hirth & Kohlstedt, 1995; Mei & Kohlstedt, 2000a, 2000b). We, therefore, imposed a maximum uncertainty of 20%. [d]Not provided by the study. We assign a conservative estimate of 10%. [e]We use the standard deviation of stresses measured at the five *hkl* peaks.

uncertainties associated with experimental variables are summarized in Table 1. The pressure-variable run PI-220 of MK00 is excluded from our analysis because of its erroneous nature (Jain et al., 2018, section 3.1). Remaining data were all obtained at similar pressures (~0.3 GPa) and cannot constrain the effect of pressure on rheology. To compare data collected with different deformation geometries, all strain rates and stresses are converted to their second invariants using the Levy-von Mises equation (Karato, 2008, chapter 3).

Whereas it is reasonable to assume that strain rates measured by different studies exhibit systematic differences, interrun biases within a study may be harder to justify. We, therefore, consider two broad possibilities for interrun biases in our data sets. In the first, we only account for possible "inter-laboratory biases" between data belonging to different studies, that is, OL-DA is divided into three data groups (denoted as OL-DA$_1$, where the subscript "1" stands for the consideration of inter-laboratory bias only) and OL-DB into four groups (OL-DB$_1$). In the second possibility, we also consider systematic errors within each study. However, there may be more than one way to decompose experimental runs into different groups. Here we only report results of the grouping that yielded the smallest misfit to data. For OL-DA, such grouping comprised the following six groups (OL-DA$_2$, where the subscript "2" denotes the consideration of both inter-laboratory bias as well as interrun bias within each study): (1) runs 4721, 4745, 4821, and 4929 of KPF86; (2) run 4,759 of KPF86; (3) run 4778 of KPF86; (4) runs PI-35, and PI-81 of HK95; (5) run PI-146 of HK95; and (6) runs PI-181, PI-360, PI-394, and PI-567 of MK00. For OL-DB, division into eight groups (OL-DB$_2$) produced the smallest misfit. Of these, six groups are identical to those of OL-DA$_1$, and the remaining two groups (all from HZK11) are as follows: (7) runs PI-1477, PI-1488, PI-1514, and PI-1543 and (8) runs PI-1519 and PI-1523.

Using our MCMC inversion scheme, we fit each of these four cases with the following two composite rheological models: (I) the parallel operation of diffusion and dislocation creep,

$$\dot{\epsilon}_{obs} = \left(\dot{\epsilon}_{diff} + \dot{\epsilon}_{dis}\right) \cdot \exp(X_m), \tag{12}$$

and (II) the parallel operation of diffusion creep, dislocation creep, and GBS,

$$\dot{\epsilon}_{obs} = \left(\dot{\epsilon}_{diff} + \dot{\epsilon}_{dis} + \dot{\epsilon}_{gbs}\right) \cdot \exp(X_m). \tag{13}$$

Here ϵ_{diff}, ϵ_{dis}, and $\dot{\epsilon}_{gbs}$ represent strain rates due to diffusion creep (equation (1)), dislocation creep (equation (3)), and GBS (equation (5)), respectively, under dry conditions. For the reason described earlier, the activation volumes are excluded from our inversion. Unlike KK08, we assume the following wide a priori bounds, to examine how flow-law parameters are actually constrained by data themselves (Jain et al., 2018): $-5 \leq p_i \leq 5$, $1 \leq n_i \leq 10$, and $0 \leq E_i \leq 1,000$, where E_i is in kJ mol^{-1}. Each MCMC output was resampled at intervals of 500–1,000, and we repeated each inversion three times with different initial guesses to confirm convergence.

We note here that a priori bounds on each flow-law parameter are usually derived either from theoretical considerations or from previous experimental results. For the grain-size exponent, in particular, only values

Table 2
Results of MCMC Inversion of Two Global Data Sets, OL-DA and OL-DB, Under Dry Conditions, for the Composite Rheological Model (12)

Mechanism	Parameters	OL-DA$_1$	OL-DA$_2$	OL-DB$_1$	OL-DB$_2$
Dry diffusion	p_1	2.07 ± 0.21	1.43 ± 0.11	2.25 ± 0.14	2.11 ± 0.15
	E_1	268 ± 146	385 ± 53	396 ± 34	370 ± 15
	A_1	$10^{4.46\pm0.23}$	$10^{7.66\pm0.13}$	$10^{8.93\pm0.13}$	$10^{7.86\pm0.15}$
Dry dislocation	n_3	4.98 ± 0.30	4.77 ± 0.16	3.72 ± 0.12	3.64 ± 0.09
	E_3	197 ± 115	188 ± 39	368 ± 28	424 ± 23
	A_3	$10^{-8.24\pm0.63}$	$10^{-8.21\pm0.34}$	$10^{0.08\pm0.27}$	$10^{2.10\pm0.20}$
Misfit	χ^2_M/N	~698	~92	~457	~306

Note. For each case, two different assumptions on interrun biases are tested. OL-DA$_1$ and OL-DB$_1$ are inversion results with only inter-laboratory biases, and OL-DA$_2$ and OL-DB$_2$ represent results with additional interrun biases. The mean values of model parameters for diffusion and dislocation creep are reported, along with their one standard deviation. Normalized misfit χ^2_M/N is also given for each case. Parameter p_1 is the grain-size exponent for diffusion creep, n_3 the stress exponent for dislocation creep, E_1 and E_3 the respective activation energies for the two mechanisms in kJ mol^{-1}, and A_1 and A_3 their respective scaling coefficients. Interrun biases are reported in Table S1 and correlation coefficients in Tables S2–S5.

between 1 and 3 are consistent with theory. Our recent analysis, however, showed that most of individual experimental runs of the studies KPF86, HK95, and MK00 were best fit with p_1 ~0 (Jain et al., 2018). Furthermore, it was suggested that global inversions could constrain p_1 to higher, more theoretically acceptable values because global data sets would encompass a wider variability in grain sizes than those explored in individual experimental runs. The wide a priori bounds on grain-size exponents are needed to test this possibility.

3.1. Results for Dry Composite Rheologies

Tables 2 and 3 summarize our global inversion results for the composite rheological models (I) (equation (12)) and (II) (equation (13)), respectively. Figure 2 shows the a posteriori probability distributions of the normalized misfit χ^2_M/N and estimated flow-law parameters for model (I), and the corresponding data fit is given in Figure 3. Results for model (II), that is, with GBS, are shown similarly in Figures 4 and 5.

Table 3
Results of MCMC Inversion of Two Global Data Sets, OL-DA and OL-DB, Under Dry Conditions, for the Composite Rheological Model (13)

Mechanism	Parameters	OL-DA$_1$/g	OL-DA$_2$/g	OL-DB$_1$/g	OL-DB$_2$/g
Dry diffusion	p_1	2.60 ± 0.15	0.98 ± 0.08	2.36 ± 0.12	1.73 ± 0.13
	E_1	320 ± 80	475 ± 38	460 ± 68	321 ± 22
	A_1	$10^{6.78\pm0.16}$	$10^{10.13\pm0.08}$	$10^{11.24\pm0.12}$	$10^{5.73\pm0.14}$
Dry dislocation	n_3	7.70 ± 0.23	5.02 ± 0.09	3.66 ± 0.04	3.82 ± 0.13
	E_3	138 ± 53	190 ± 13	358 ± 37	400 ± 39
	A_3	$10^{-15.96\pm0.46}$	$10^{-8.65\pm0.20}$	$10^{-0.17\pm0.06}$	$10^{0.86\pm0.29}$
Dry GBS	p_5	-0.65 ± 0.07	4.29 ± 0.68	-1.84 ± 1.44	4.63 ± 0.29
	n_5	1.02 ± 0.01	1.04 ± 0.03	4.99 ± 1.47	3.80 ± 0.46
	E_5	951 ± 66	408 ± 253	732 ± 197	692 ± 92
	A_5	$10^{23.64\pm0.11}$	$10^{10.38\pm0.53}$	$10^{5.79\pm5.39}$	$10^{14.93\pm1.07}$
Misfit	χ^2_M/N	~589	~90	~428	~217

Note. GBS = grain boundary sliding. OL-DA$_1$/g and OL-DB$_1$/g are inversion results with only inter-laboratory biases, and OL-DA$_2$/g and OL-DB$_2$/g represent results with additional interrun biases. The mean values of model parameters for diffusion creep, dislocation creep, and grain boundary sliding accommodated by dislocation creep (GBS) are reported, along with their one standard deviation. Normalized misfit χ^2_M/N is also given for each case. Parameter p_i is the grain-size exponent, n_i the stress exponent, E_i the activation energy in kJ mol^{-1}, and A_i the scaling coefficient for the ith deformation mechanism, where $i = 1$ represents diffusion creep, $i = 3$ dislocation creep, and $i = 5$ GBS. Interrun biases are reported in Table S6 and correlation coefficients in Tables S7–S10.

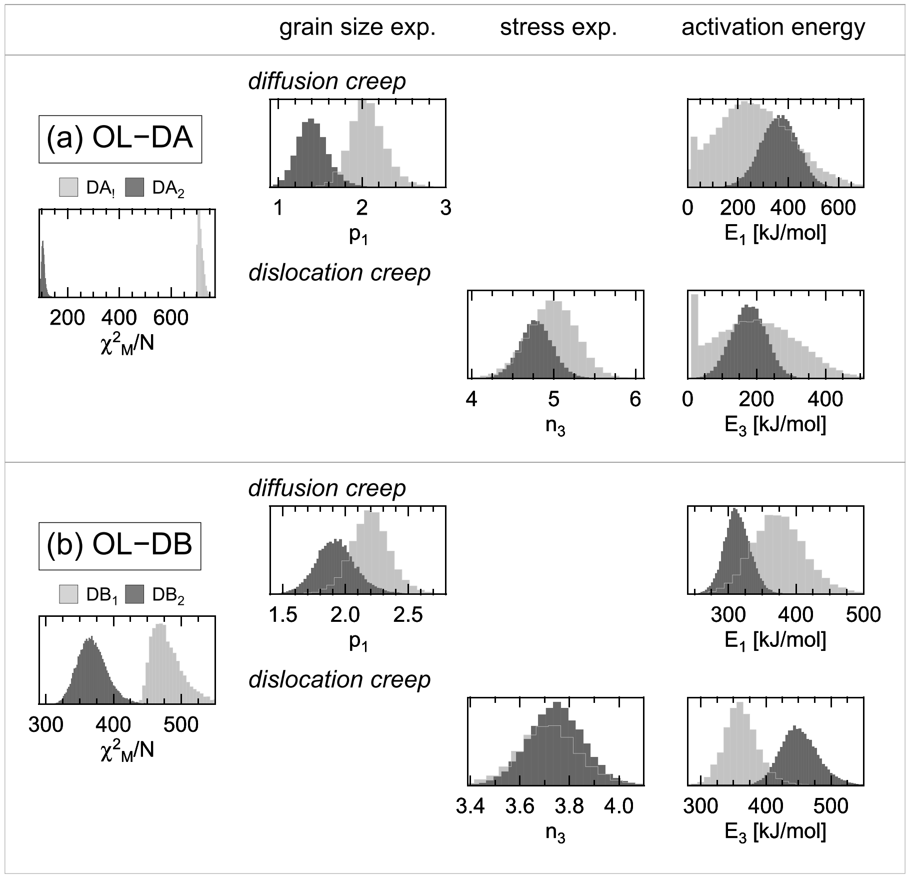

Figure 2. Histograms of Markov chain Monte Carlo solutions from four different simulations with dry data. OL-DA represents data compiled from the three studies KPF86, HK95, and MK00. Simulations DA_1 (light gray) and DA_2 (dark gray) are global inversions of the data set OL-DA that take three inter-laboratory and six interrun biases, respectively, into account. Similarly, OL-DB represents data compiled from the three aforementioned studies and HZK11, and simulations DB_1 and DB_2 are inversions with four inter-laboratory and eight interrun biases, respectively. All data sets are analyzed for the composite rheological model (I) (equation (12)) under dry conditions with wide a priori bounds. The a posteriori probability distributions of χ^2_M/N and estimated flow-law parameters for diffusion and dislocation creep are shown for each simulation.

OL-DA and OL-DB yield distinctly different estimates on some of flow-law parameters for both composite rheological models. For example, in case of model (I), OL-DA constrains the stress exponent for dislocation creep n_3 at 5.0 ± 0.3 (uncertainty is 1σ), but OL-DB returned an estimate of 3.7 ± 0.1; the two estimates do not overlap even at 3σ level. OL-DB also yields tighter constraints on most of flow-law parameters for diffusion and dislocation creep, especially the activation energies E_1 and E_3 (Figures 2a and 4a, compare light versus dark gray histograms), possibly because it contains more data points, and HZK11 data are often associated with smaller uncertainties. The effect of including HZK11 data, as revealed by such differences between OL-DA and OL-DB, will be discussed in the next section.

Global estimates on flow-law parameters also vary with different assumptions on interrun biases. For example, the grain-size exponent for diffusion creep is lower for OL-DA_2 than OL-DA_1. This is most likely because data groups in OL-DA_2 are subsets of those in OL-DA_1 and, therefore, encompass a narrower range of grain sizes, reducing the sensitivity of strain rates to grain sizes (Jain et al., 2018, section 3.3). Shift in the estimate on p_1 between the two cases could affect estimates on other parameters as well because of correlation between model parameters (Tables S2–S9). However, the remaining data sets tightly constrain p_1 at ~ 2 (Figures 2 and 4), which is indicative of the dominance of Nabarro-Herring creep in these experiments.

Our results also suggest that the currently available data cannot uniquely constrain the flow-law parameters for GBS. For example, peaks are poorly resolved in the probability distributions of p_5 yielded by OL-DA_2/g

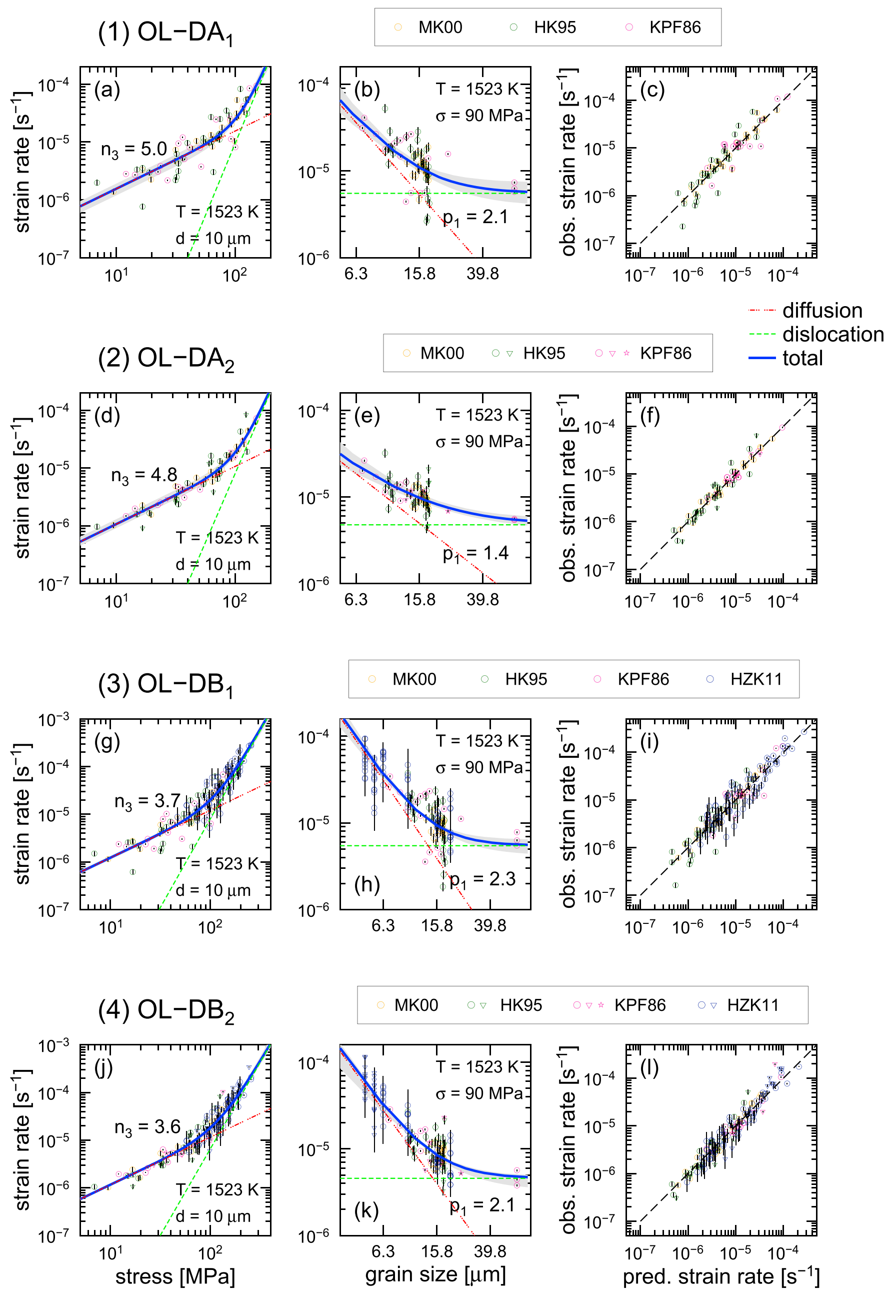

Figure 3. Comparison of experimental data with the estimated flow law for four Markov chain Monte Carlo simulations with dry data. All data sets are analyzed for the composite rheological model (equation (12)) with wide a priori bounds. OL-DA$_1$ and OL-DA$_2$ are our inversion results for global data set OL-DA with three inter-laboratory and six interrun biases, respectively. OL-DB$_1$ and OL-DB$_2$ similarly represent our inversion results for global data set OL-DB with four inter-laboratory and eight interrun biases, respectively. Panels (a, d, g, and j) represent the fit to data in the stress versus strain rate space. Observed strain rates (symbols) are corrected for interrun biases and normalized to the temperature of 1,523 K and the grain size of 10 μm using the mean values of the relevant flow-law parameters (Table 2). The mean estimate on n_3 is mentioned. Panels (b, e, h, and k) represent the fit in the grain size versus strain rate space. Observed strain rates are corrected for interrun biases and normalized to the temperature of 1,523 K and the stress of 90 MPa. The mean value of p_1 is shown for each case. Mean model predictions are represented by blue line, and the 90% confidence interval is shaded in gray. Individual contributions of diffusion (red dashed line) and dislocation creep (green dotted line) are also plotted. Panels (c, f, i, and l) compare the observed strain rates, corrected for interrun bias, with those predicted by the mean model at corresponding experimental conditions. All strain rates were measured at 0.3-GPa pressure. Error bars denote experimental uncertainties in strain rate. Different symbols for data of the same study in OL-DA$_2$ and OL-DB$_2$ represent different data groups. See also Figure S6.

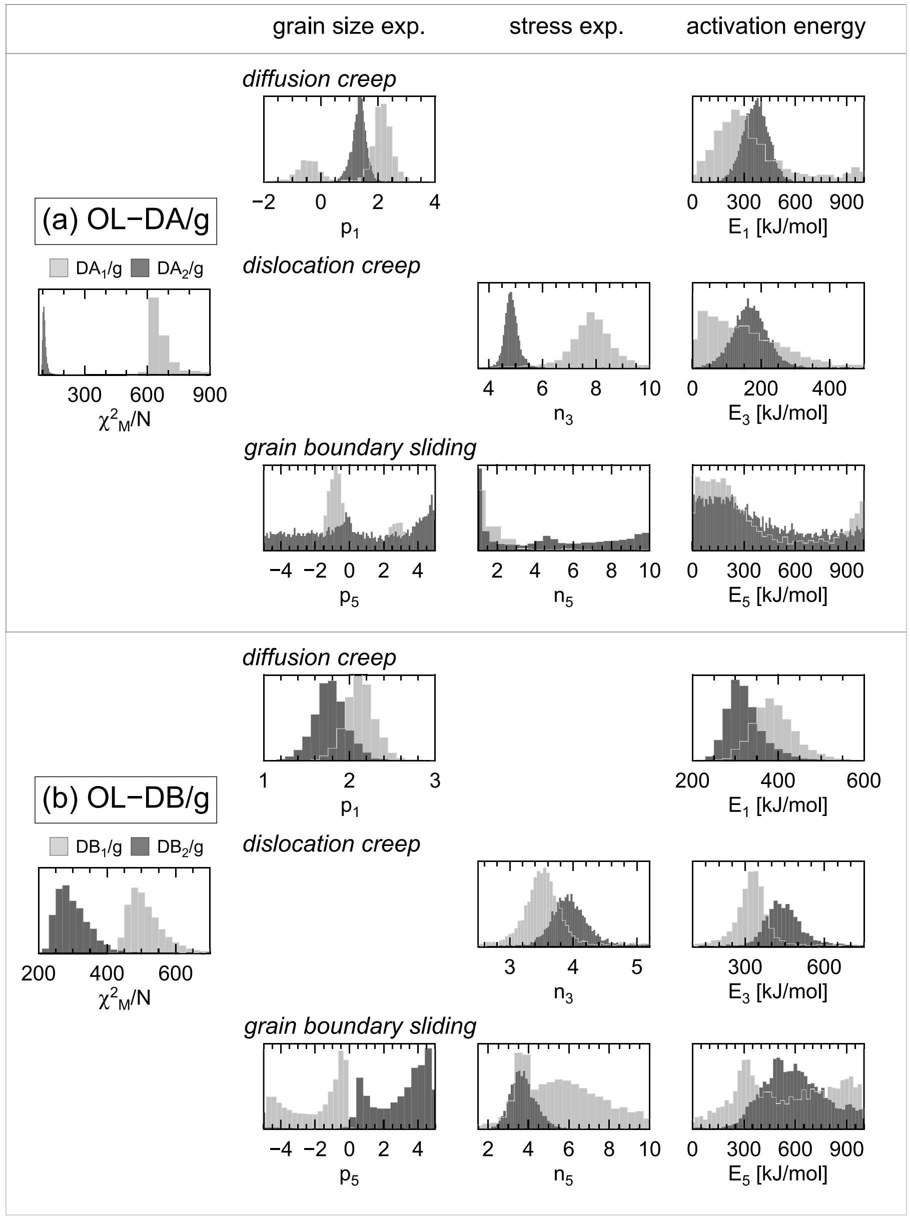

Figure 4. Same as Figure 2 but for the composite rheological model (II) (equation (13)) under dry conditions. Here simulation DA_1/g (light gray) and DA_2/g (dark gray) represent our inversion results for global data set OL-DA with three inter-laboratory and six interrun biases, respectively. Simulations DB_1/g and DB_2/g similarly represent our inversion results for global data set OL-DB with four inter-laboratory and eight interrun biases, respectively. The a posteriori probability distributions of the estimated flow-law parameters for grain boundary sliding are also shown.

(the suffix "/g" denotes inversion results for data set OL-DA_2 for model (II), that is, with GBS) and OL-DB_2/g, and E_5 is only loosely constrained in all cases (Figures 4a and 4b). The value of p_5, in particular, varies widely from $p_5 < 0$ for cases OL-DA_1/g and OL-DB_1/g to $p_5 > 3$ for cases OL-DA_2/g and OL-DB_2/g. This nonuniqueness in the estimates on p_5 may be explained by the significant correlation between p_5 and other flow-law parameters (Tables S7–S9), because of which p_5 changes when constraints on other flow-law parameters change from one case to another. More important, the contribution of GBS to the observed deformation is largely trivial (Figure 5), and even though χ^2_M/N for model (I) is greater than that for model (II) (e.g., Figures 2b and 4b), we find that both models fit data equally well (see section S3), indicating that the given data can be explained without calling for GBS.

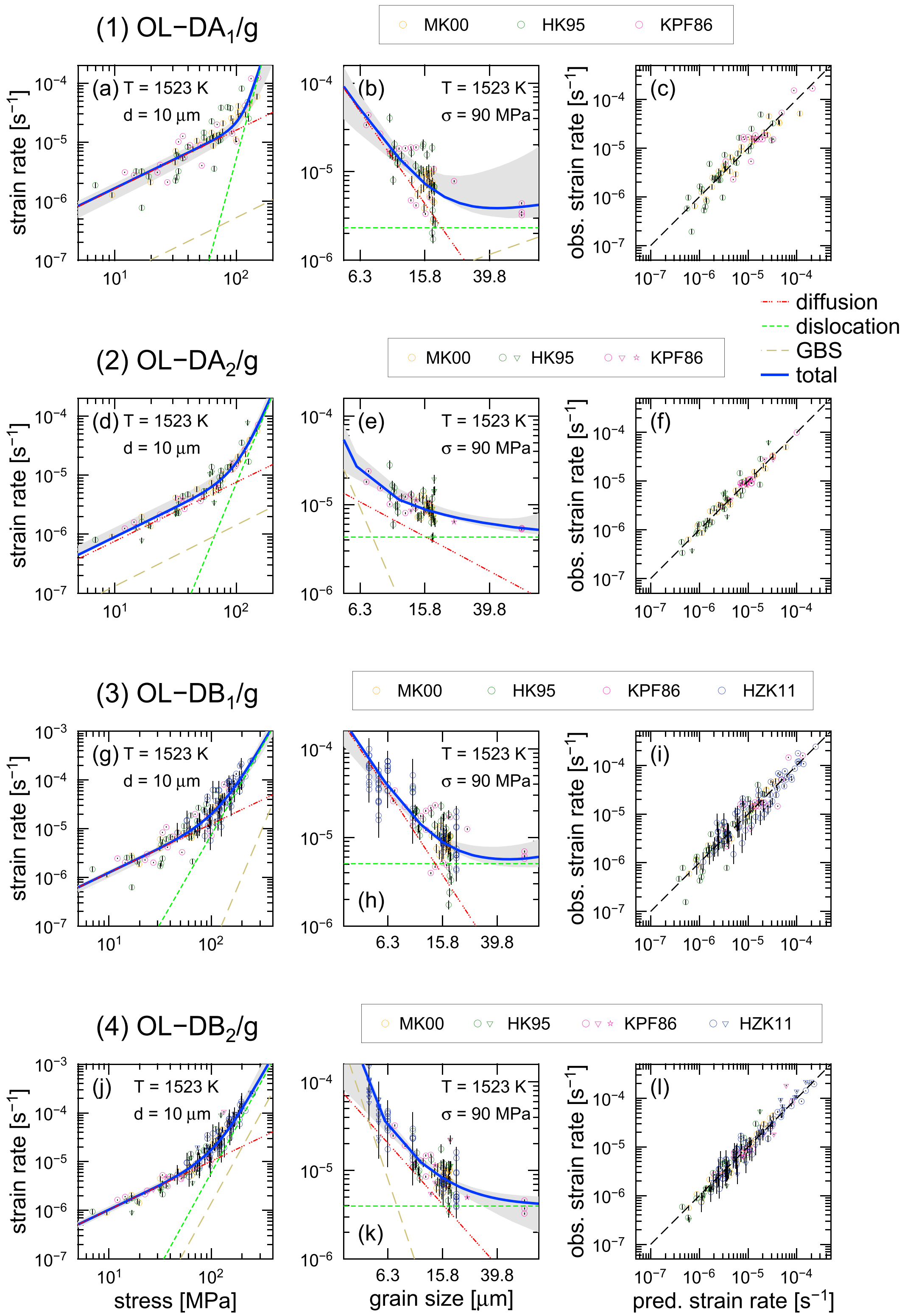

Figure 5. Same as Figure 3 but for the composite rheological model (II) (equation (13)). Here OL-DA$_1$/g and OL-DA$_2$/g represent our inversion results for global data set OL-DA with three inter-laboratory and six interrun biases, respectively. OL-DB$_1$/g and OL-DB$_2$/g represent our results for global data set OL-DB with four inter-laboratory and eight interrun biases, respectively (Table 3). Contribution of GBS to the total strain rate is shown as khaki dashed line. See also Figure S7.

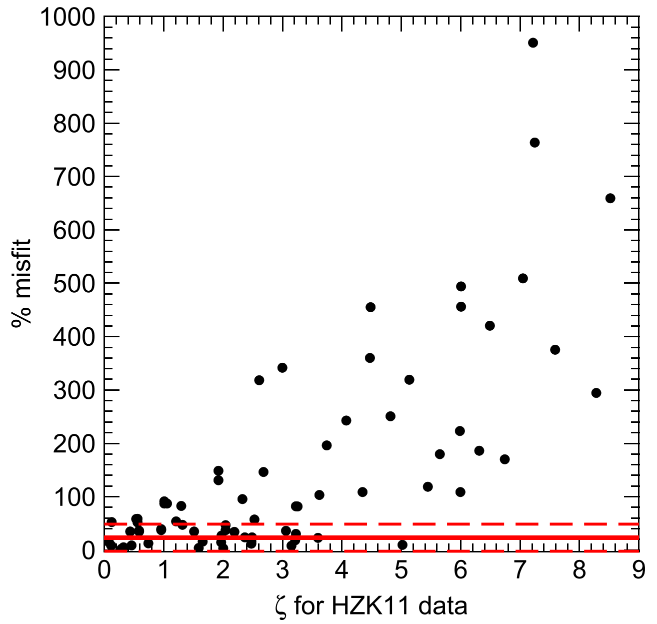

Figure 6. Plot of percent misfit between the observed strain rates ($\dot{\epsilon}_{\rm obs}$) of HZK11 and those predicted at the same conditions ($\dot{\epsilon}_{pred}$) by the composite rheological model OL-DA$_2$. Percent misfit is calculated as $\left|1 - \dot{\epsilon}_{pred}/\dot{\epsilon}_{\rm obs}\right| \times 100$. HZK11 data are arranged in ascending order of their condition difference ζ (see section 3.2). Average misfit between the same model and the OL-DA$_2$ data (red solid line) is also shown, along with its one standard deviation (red dashed lines).

Finally, all composite rheological models reported here are associated with large misfits ($\chi^2_{\rm M}/N \gg 1$). The models that take more interrun biases into account (OL-DA$_2$, OL-DB$_2$, OL-DA$_2$/g, and OL-DB$_2$/g) yield smaller $\chi^2_{\rm M}/N$ (Figures 2a, 2b, 4a, and 4b, light versus dark gray histograms) and fit experimental data better (e.g., Figures 3d–3f vs. Figures 3a–3c). However, $\chi^2_{\rm M}/N$ is greater than 100 even for these cases. Such large $\chi^2_{\rm M}/N$ may indicate that true data uncertainties are greater than reported (Jain et al., 2018). Another possibility is internal inconsistencies in data. In particular, higher $\chi^2_{\rm M}/N$ for OL-DB$_2$ and OL-DB$_2$/g than OL-DA$_2$ and OL-DA$_2$/g, respectively, even though OL-DB is a super set of OL-DA, is difficult to explain without assuming incompatibility between the OL-DA and HZK11 data. This is a significant issue from the perspective of reanalysis, so we will pursue it in the following section.

3.2. Understanding the Difference Between OL-DA and OL-DB

Possible incompatibility between the OL-DA and HZK11 data can be identified by assessing how closely the inversion results of the OL-DA data fit HZK11 data. As a representative case, we compare the observed strain rates $\dot{\epsilon}_{\rm obs}$ of HZK11 with those predicted, $\dot{\epsilon}_{\rm pred}$, by model (I) (equation (12)), assuming the flow-law parameters for OL-DA$_2$ (Figure 6). The misfit is larger than 100% for most of HZK11 data.

We can further ask whether this misfit originates in different experimental conditions between the OL-DA and HZK11 data. To this end, we define the condition difference, ζ_i, for the ith data point of HZK11 as

$$\zeta_i = \min_{\forall j \in [1..N_A]} \left|\frac{T_i - T_j}{\Delta T}\right| + \left|\frac{\sigma_i - \sigma_j}{\Delta\sigma}\right| + \left|\frac{d_i - d_j}{\Delta d}\right|, \tag{14}$$

where subscripts i and j denote the ith data point of HZK11 and jth data point of the OL-DA data set, respectively, and N_A is the total number of data points in OL-DA. Given the spread of experimental conditions (Figure 1), we set $\Delta T = 25$ K, $\Delta\sigma = 20$ MPa, and $\Delta d = 5$ μm. The parameter ζ_i quantifies the difference in experimental conditions between each HZK11 data point and the one with the most similar conditions in the OL-DA data, with a smaller value of ζ_i corresponding to greater similarity. Figure 6 shows that the HZK11 data even with small condition difference ($\zeta_i < 1$) exhibit large misfits, implying that the incompatibility cannot be attributed solely to difference in experimental conditions. It is beyond the scope of this study to investigate the cause of incompatibility, but a plausible reason could be the overestimation of sample grain sizes by KPF86, HK95, and MK00, as suggested by HZK11 (section 6.1 and Appendix B of HZK11). Figure 7 of HZK11 indicates that the difference in grain sizes measured by the lower- and the higher-resolution techniques used by the older studies and HZK11, respectively, is not a constant factor; therefore, its influence may not be entirely accounted for by inter-laboratory biases in our inversion scheme, making data of HZK11 incompatible with the fine-grained data of OL-DA.

3.3. Comparison With Previous Studies

As discussed in section 3.1, global data sets considered here do not constrain all parameters uniquely. Below we assess the extent to which our inversion results could resolve the discrepancies in previously published estimates on flow-law parameters under dry conditions.

For the grain-size exponent for diffusion creep in olivine, a number of experimental studies have favored a value of 3 (e.g., Faul & Jackson, 2007; Hirth & Kohlstedt, 1995, 2003; Mei & Kohlstedt, 2000a) over 2 (e.g., KPF86); both values are consistent with theory (2 for bulk diffusion and 3 for grain-boundary diffusion). The reanalysis of individual experimental runs of KPF86, HK95, and MK00a mostly yielded $p_1 \sim 0$ with large 1σ bounds because these data included only a narrow range of grain sizes (Jain et al., 2018). Our global data sets, which span a wider range of grain sizes, instead constrain p_1 tightly at ~2 (Table 2), questioning the validity of the common assumption of $p_1 = 3$ in geodynamics and experimental rock mechanics (e.g., Alisic et al., 2012; Hansen et al., 2011). Furthermore, the effective diffusion coefficient for olivine predicted by our results agrees with the results of KPF86 and indicates that diffusion creep in olivine may be controlled by the bulk diffusion of Mg(Fe) ions (section S4).

Table 4
MCMC Inversion Results of Two Global Data Sets, OL-WA and OL-WB, Under Wet Conditions, for the Composite Rheological Model (12)

Mechanism	Parameters	OL-WA$_1$	OL-WA$_2$	OL-WB$_1$	OL-WB$_2$
Wet diffusion	p_2	1.74 ± 0.13	1.92 ± 0.08	1.74 ± 0.12	1.91 ± 0.08
	r_2	0.85 ± 0.25	0.41 ± 0.13	0.84 ± 0.26	0.69 ± 0.17
	E_2	364 ± 61	400 ± 36	362 ± 60	384 ± 35
	V_2	7.73 ± 12.64	-28.08 ± 3.71	6.75 ± 13.23	-13.35 ± 6.48
	A_2	$10^{5.49 \pm 0.76}$	$10^{7.90 \pm 0.41}$	$10^{5.56 \pm 0.47}$	$10^{6.46 \pm 0.45}$
Wet dislocation	n_4	4.43 ± 0.33	3.49 ± 0.13	4.45 ± 0.32	3.48 ± 0.12
	r_4	1.99 ± 0.02	1.93 ± 0.08	2.00 ± 0.02	1.95 ± 0.06
	E_4	430 ± 188	372 ± 46	425 ± 190	375 ± 48
	V_4	27.65 ± 8.56	19.25 ± 7.13	27.96 ± 8.12	18.27 ± 7.53
	A_4	$10^{-4.35 \pm 0.71}$	$10^{-4.03 \pm 0.35}$	$10^{-4.47 \pm 0.83}$	$10^{-4.18 \pm 0.34}$
Misfit	χ^2_M/N	$\sim$910	$\sim$130	$\sim$886	$\sim$128

Note. MCMC = Markov chain Monte Carlo. For each case, two different assumptions on interrun biases are tested. OL-WA$_1$ and OL-WB$_1$ are inversion results with only inter-laboratory biases, and OL-WA$_2$ and OL-WB$_2$ represent results with additional interrun biases. The mean values of model parameters for diffusion and dislocation creep are reported, along with their one standard deviation. Normalized misfit χ^2_M/N is also given for each case. Parameter p_2 is the grain-size exponent for diffusion creep, n_4 the stress exponent for dislocation creep, r_2 and r_4 the respective water-content exponents for the two mechanisms, E_2 and E_4 their activation energies in kJ mol^{-1}, V_2 and V_4 their activation volumes in cm^3 mol^{-1}, and A_2 and A_4 their scaling coefficients. Interrun biases are reported in Table S12 and correlation coefficients in Tables S13–S16.

Note that theory also allows a grain-size exponent of 1 for deformation controlled by interface reaction, and two cases, OL-DA$_2$ and OL-DA$_2$/g, do return $p_1 < 1.5$. However, because the remaining six cases considered here constrain $p_1 \sim 2$, it is more likely that the lower value of p_1 yielded by the two cases is not an indication of interface reaction control but rather a consequence of the smaller range of grain sizes spanned by each data group in the OL-DA$_2$ data set (section 3.1). Accordingly, $p_1 < 1.5$ returned by OL-DA$_2$ and OL-DA$_2$/g may not be acceptable. The success of global data sets in constraining the value of p_1 underscores the importance of analyzing data with a wide range of grain sizes. Surprisingly, global inversions conducted by KK08 on the data set OL-DA$_1$ could not constrain p_1 within the expected range of 1–3. The differences between their inversion results and ours will be discussed in section 5.2.

For the stress exponent for dislocation creep, whereas many studies have reported values between 3 and 3.6 (e.g., Chopra and Paterson, 1984; KPF86; HK95; MK00; Durham et al., 2009), some studies have published higher estimates on n_3, for example, $\sim$5 (Carter & Ave'Lallemant, 1970; Poirier, 1985) and 3–5 for olivine single crystals (Bai et al., 1991; Mullet et al., 2015). Our estimates too range from 3.6 to 5. Only OL-DA$_1$/g yielded $n_3 \sim 8$, which is much higher than expected. Such a high exponent is often indicative of exponential creep instead of dislocation creep (e.g., Faul et al., 2011).

For the activation energy for diffusion creep, our global estimates overlap with previously published values of $\sim$300 kJ mol^{-1} (HK95) and 375 ± 30 kJ mol^{-1} (Hirth & Kohlstedt, 2003). Only two cases, that is, OL-DA$_2$/g and OL-DB$_1$/g, returned higher values of E_1. In contrast, all cases yield estimates on the activation energy for dislocation creep that are much lower than the conventionally accepted value of $\sim$530 kJ mol^{-1} (e.g., Chopra & Paterson, 1984; Karato & Jung, 2003; Mei & Kohlstedt, 2000b). Also, the OL-DA data collectively constrain E_3 considerably below E_1, which is opposite to the results published by HK95 and MK00. However, in the absence of stronger theoretical bounds on E_1 and E_3, all our estimates are plausible.

The flow-law parameters for GBS are neither uniquely constrained by theory (e.g., Langdon, 2006; 2009) nor by previous experimental studies (e.g., Hirth & Kohlstedt, 2003; Hansen et al., 2011). HZK11, in particular, fit their data for a composite flow law with diffusion creep and GBS and obtained $p_5 = 0.7$, $n_5 = 3$, and $E_5 = 445$ kJ mol^{-1}. Our reanalysis of their data returned similar estimates on the flow-law parameters for GBS (section S5, case 1). Our global inversion results for GBS are, however, not consistent with published estimates. OL-DA$_1$/g and OL-DB$_1$/g returned $p_5 < 0$, which may not be acceptable because theoretical studies indicate

Table 5
MCMC Inversion Results of Two Global Data Sets, OL-WA and OL-WB, Under Wet Conditions, for the Composite Rheological Model (13)

Mechanism	Parameters	OL-WA$_1$/g	OL-WA$_2$/g	OL-WB$_1$/g	OL-WB$_2$/g
Wet diffusion	0pt p_2	1.68 ± 0.10	1.95 ± 0.09	1.69 ± 0.09	1.97 ± 0.04
	r_2	1.14 ± 0.21	0.48 ± 0.13	1.10 ± 0.23	0.82 ± 0.20
	E_2	333 ± 63	409 ± 32	331 ± 47	375 ± 24
	V_2	18.68 ± 7.95	-24.81 ± 7.01	16.33 ± 8.80	-8.88 ± 7.40
	A_2	$10^{3.52\pm0.70}$	$10^{8.01\pm0.47}$	$10^{3.84\pm0.76}$	$10^{5.88\pm0.55}$
Wet dislocation	n_4	6.04 ± 2.14	3.43 ± 0.08	4.12 ± 1.76	5.15 ± 1.91
	r_4	0.06 ± 1.28	1.93 ± 0.04	0.34 ± 1.38	1.24 ± 1.34
	E_4	243 ± 213	351 ± 29	257 ± 207	368 ± 269
	V_4	-4.10 ± 22.49	11.69 ± 12.25	-11.15 ± 17.92	4.10 ± 16.90
	A_4	$10^{-12.42\pm7.56}$	$10^{-4.74\pm0.27}$	$10^{-11.40\pm18.40}$	$10^{-7.20\pm3.82}$
Wet GBS	p_6	0.70 ± 0.55	1.99 ± 1.62	0.71 ± 0.47	1.07 ± 1.47
	n_6	4.47 ± 0.76	5.11 ± 2.15	4.38 ± 0.81	5.53 ± 2.53
	r_6	1.78 ± 0.72	-0.34 ± 1.35	1.76 ± 0.79	1.12 ± 1.59
	E_6	566 ± 165	653 ± 289	575 ± 166	345 ± 183
	V_6	27.73 ± 6.36	7.06 ± 19.18	27.92 ± 5.48	3.17 ± 18.85
	A_6	$10^{1.62\pm3.67}$	$10^{8.37\pm6.50}$	$10^{2.46\pm3.96}$	$10^{-7.93\pm3.59}$
Misfit	χ^2_M/N	~926	~131	~928	~129

Note. GBS = grain boundary sliding; MCMC = Markov chain Monte Carlo. For each case, two different assumptions on interrun biases are tested. OL-WA$_1$/g and OL-WB$_1$/g are models with only inter-laboratory biases, and OL-WA$_2$/g and OL-WB$_2$/g represent results with additional interrun biases. The mean values of model parameters for diffusion creep, dislocation creep, and grain boundary sliding accommodated by dislocation creep (GBS) are reported, along with their one standard deviation. Normalized misfit χ^2_M/N is also given for each case. Parameter p_i is the grain-size exponent, n_i the stress exponent, r_i the water content exponent, E_i the activation energy in kJ mol^{-1}, V_i the activation volume in cm^3 mol^{-1}, and A_i the scaling coefficient for the ith deformation mechanism, where $i = 2$ represents diffusion creep, $i = 4$ dislocation creep, and $i = 6$ GBS. Interrun biases are reported in Table S17 and correlation coefficients in Tables S18–S21.

$p_5 > 0$ (e.g., Langdon, 1994). Inversion results for model (II) suggested by the other two cases may be plausible, given our limited understanding of this mechanism.

Based on our discussion thus far, we find that our inversion results for the composite rheological model (I), except those returned by OL-DA$_2$, are plausible, and discrepancies between different cases suggest the limitation of available experimental data. For the composite rheological model (II), only results for OL-DB$_2$/g seem acceptable.

4. Reanalysis of Wet Experimental Data

We now reanalyze experimental data for olivine aggregates under wet conditions reported by KPF86, MK00, Jung et al. (2006; J06), and Ohuchi et al. (2015; O15). Again, we consider two global data sets, OL-WA and OL-WB (where the "W" stands for wet olivine rheology); OL-WA contains all data of the first three studies, and OL-WB includes all data of OL-WA and the wet runs of O15. The OL-WA data encompass a wide range of stresses (3–300 MPa), temperatures (1,393–1,573 K), and grain sizes (12–60 μm). Whereas the experiments of KPF86 and MK00 were conducted at pressures of ~0.3 GPa, those of J06 were done at pressures up to 2 GPa. The addition of O15 data to the OL-WA data set extends the pressure range to ~6 GPa. Note that run PI-204 of MK00 is excluded from our global analysis because of problems with its data similar to run PI-220 (Jain et al., 2018, section 3.1).

Similar to our analysis of dry data, we also test two assumptions on interrun biases. To account for inter-laboratory biases, OL-WA is decomposed into three data groups (OL-WA$_1$), each group comprising data of a different study, and OL-WB into four groups (OL-WB$_1$). To account for interrun biases within each study, we consider OL-WA$_2$ and OL-WB$_2$. OL-WA$_2$ represents the following nine groups of runs: (i) runs PI-107, PI-295, PI-351, PI-372, and PI-569 of MK00; (ii) runs PI-184, PI-186, PI-308, and PI-333 of MK00; (iii) runs PI-232 and

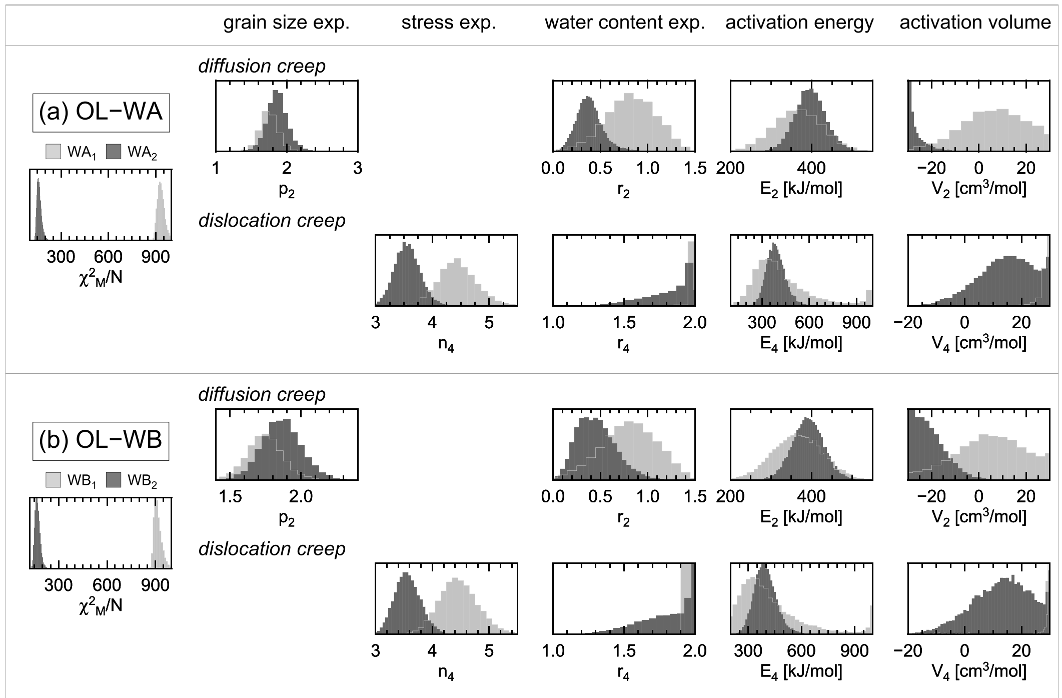

Figure 7. Histograms of Markov chain Monte Carlo solutions from four different simulations with wet data. OL-WA represents data compiled from the three studies KPF86, MK00, and J06. Simulations WA$_1$ (light gray) and WA$_2$ (dark gray) are global inversions of the data set OL-WA that take three inter-laboratory and nine interrun biases, respectively, into account. Similarly, OL-WB represents data compiled from the three aforementioned studies and the wet runs of O15, and simulations WB$_1$ and WB$_2$ are inversions with four inter-laboratory and 10 interrun biases, respectively. All data sets are analyzed for the composite rheological model (I) (equation (12)) with wide a priori bounds. The a posteriori probability distributions of χ^2_M/N and estimated flow-law parameters for diffusion and dislocation creep are shown for each simulation.

PI-258 of MK00; (iv) runs PI-507, PI-544, and PI-568 of MK00; (v) runs 4677, 4678, 4682, and 4692 of KPF86; (vi) runs 4690 and 4927 of KPF86; (vii) runs 4714 and 4814 of KPF86; (viii) runs 4786 and 4836 of KPF86; and (ix) all data of J06. OL-WB$_2$ contains 10 groups of runs, nine of which are identical to the groups in OL-WA$_2$, and the tenth group comprises O15 data.

Each of the four cases is analyzed for the two composite rheological models, that is, model (I) (equation (12)) and model (II) (equation (13)), where $\dot{\epsilon}_{dif}$, $\dot{\epsilon}_{dis}$, and $\dot{\epsilon}_{gbs}$ in equations (12) and (13) represent strain rates due to diffusion creep (equation (2)), dislocation creep (equation (4)), and GBS (equation (6)), respectively, under wet conditions. The following wide a priori bounds are assumed: $-5 \le p_i \le 5$, $1 \le n_i \le 10$, $-2 \le r_1 \le 2$, $0 \le E_i \le 1,000$, and $-30 \le V_i \le 30$, where E_i is in kJ mol^{-1} and V_i in cm^3 mol^{-1}. The MCMC outputs were resampled at intervals of 1,000–1,500, and each inversion was repeated three times with different initial guesses to confirm convergence. The resampling intervals are longer than those for dry cases; this reflects that inversion for wet composite rheology is slightly more involved.

4.1. Results for Wet Composite Rheologies

Tables 4 and 5 report inversion results for composite rheological models (I) and (II), respectively. Figure 7 shows the a posteriori probability distributions of χ^2_M/N and flow-law parameters for model (I), and Figure 8 shows the goodness of fit between observed data and model predictions. Figures 9 and 10 display our results for model (II).

OL-WA and OL-WB appear to yield similar estimates on flow-law parameters, perhaps because the OL-WA data are significantly more in number than O15 data, and therefore, constraints imposed by the former dominate. Consequently, both cases suggest a value of ∼2 for the grain-size exponent for diffusion creep. Both also prefer a value higher than 2 for the water-content exponent for dislocation creep (Figures 7a and 7b). OL-WA and OL-WB return overlapping constraints on the activation energies E_2 and E_4 for diffusion and dislocation creep, respectively.

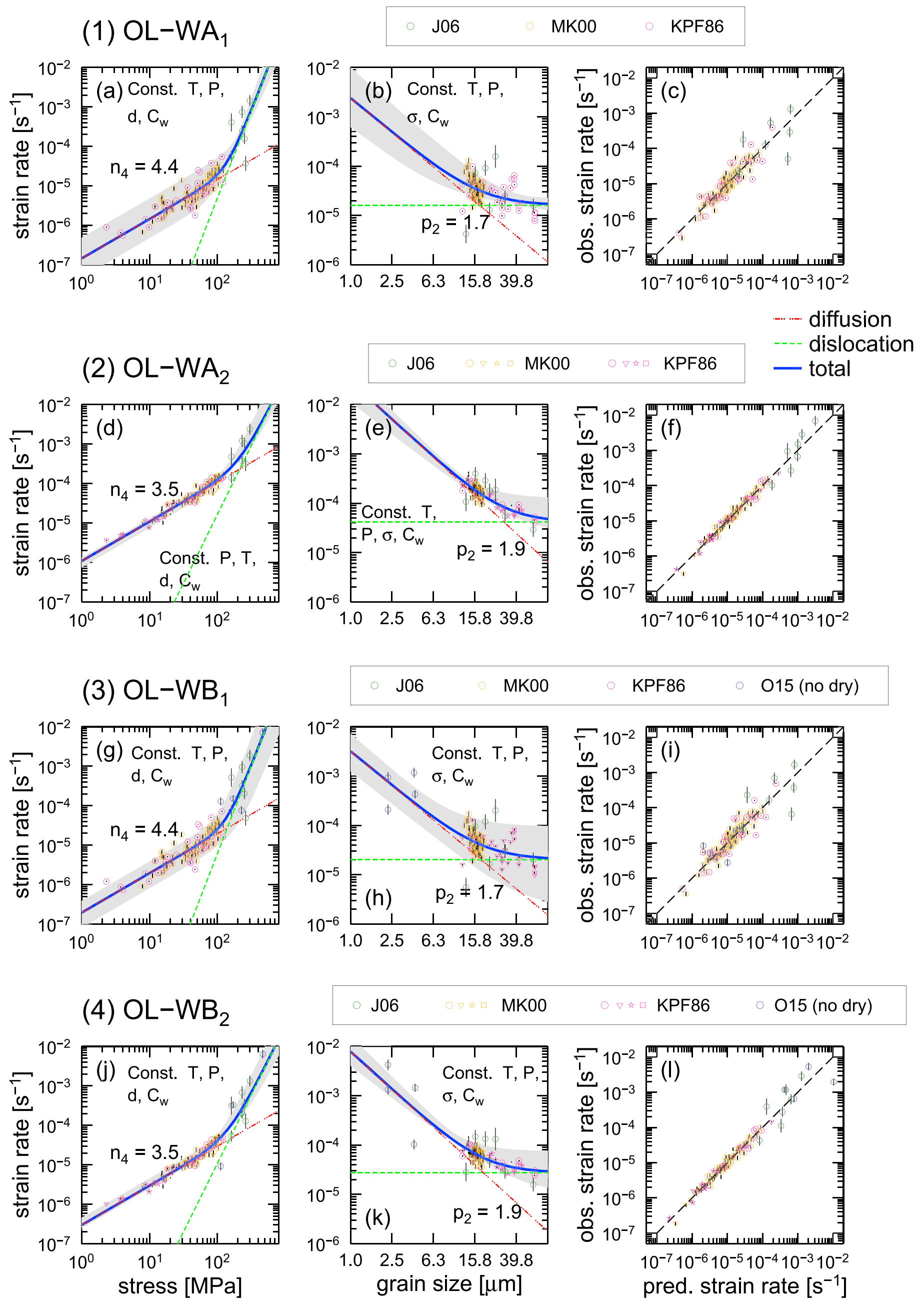

Figure 8. Comparison of experimental data with the estimated flow law for four Markov chain Monte Carlo simulations with wet data. All data sets are analyzed for the composite rheological model (I) (equation (12)) with wide a priori bounds. OL-WA$_1$ and OL-WA$_2$ represent our inversion results for data set OL-WA, considering three inter-laboratory and nine interrun biases, respectively, and OL-WB$_1$ and OL-WB$_2$ are our inversion results for OL-WB with four inter-laboratory and 10 interrun biases, respectively. Panels (a, d, g, and j) represent the fit to observed data in the stress versus strain rate space. The mean value of n_4 obtained in each case is shown. Panels (b, e, h, and k) represent the fit in the grain size versus strain rate space. The mean estimate on p_2 for each case is shown. Mean model predictions are represented by blue line and the 90% confidence intervals shaded in gray. Individual contributions of diffusion (red dashed line) and dislocation creep (green dotted line) are also plotted. Normalizing conditions are $T = 1,523$ K, $P = 1$ GPa, $d = 16$ μm, $\sigma = 130$ MPa, and $C_W = 900$ ppm H/Si. In each panel, observed strain rates are normalized using the mean values of the relevant flow-law parameters (Table 4). Panels (c, f, i, and l) compare the observed strain rates with mean model predictions at corresponding experimental conditions. In all panels (a–l), observed strain rates are corrected for interrun biases. Error bars denote experimental uncertainties in strain rate. Different symbols for data of the same study in OL-WA$_2$ and OL-WB$_2$ represent different data groups. See also Figure S12.

10.1029/2018JB016558

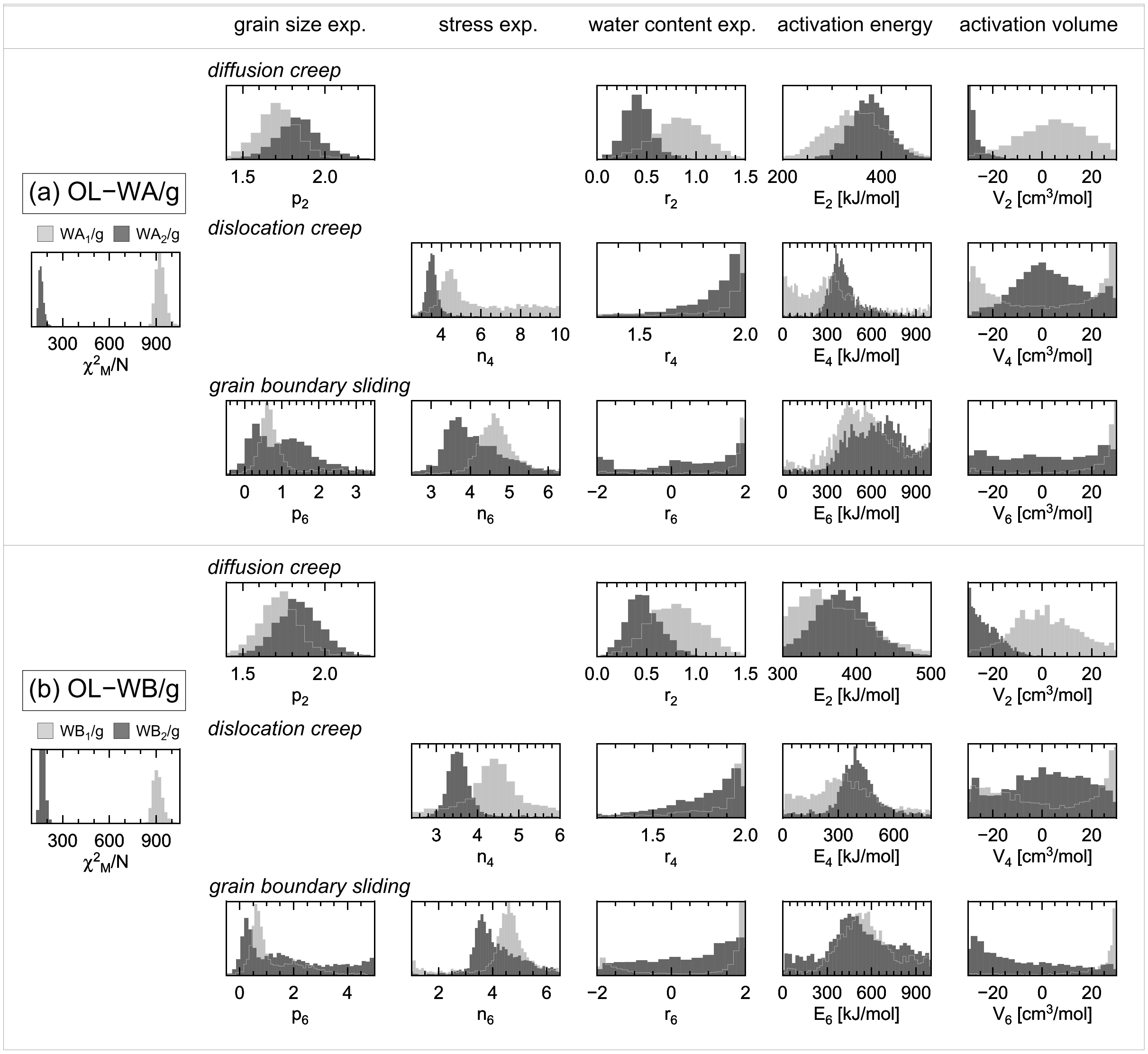

Figure 9. Same as Figure 7 but for the composite rheological model (II) (equation (13)) under wet conditions. Simulation WA$_1$/g (light gray) and WA$_2$/g (dark gray) represent our inversion results for global data set OL-WA with three inter-laboratory and nine interrun biases, respectively. Simulations WB$_1$/g and WB$_2$/g similarly represent our inversion results for global data set OL-WB with four inter-laboratory and 10 interrun biases, respectively. The a posteriori probability distributions of the flow-law parameters for GBS are also shown for each simulation.

Our assumption on interrun biases influences our results. For example, whereas OL-WA$_1$ constrains the water-content exponent for diffusion creep r_2 at 0.85, OL-WA$_2$ yields $r_2 \sim 0.4$, and the two estimates do not overlap at 1σ level. Inversions with further data division (OL-WA$_2$, OL-WB$_2$, OL-WA$_2$/g, and OL-WB$_2$/g) yield tighter constraints on the flow-law parameters for diffusion and dislocation creep (e.g., Figures 7a and 7b, compare light versus dark gray histograms) but more loose constraints on the flow-law parameters for GBS (e.g., Figure 9a). However, for models (I) and (II), the cases that include more interrun biases produce better fit to experimental data (e.g., Figures 8d–8f vs. Figures 8a–8c) as they yield smaller χ^2_M/N than the cases with only inter-laboratory biases (Figures 7a, 7b, 9a, and 9b).

The activation volumes V_2 and V_4 for diffusion and dislocation creep, respectively, are not well constrained by any data set considered here (e.g., Figure 7a). This may be a result of insufficient high-pressure data. Large uncertainties associated with high-pressure data (Table 1) could also blur constraints on V_i. Additionally, high-pressure data of J06 and O15 are likely to belong exclusively to the dislocation creep regime because of high stresses; therefore, they may not reliably constrain pressure effects on diffusion creep.

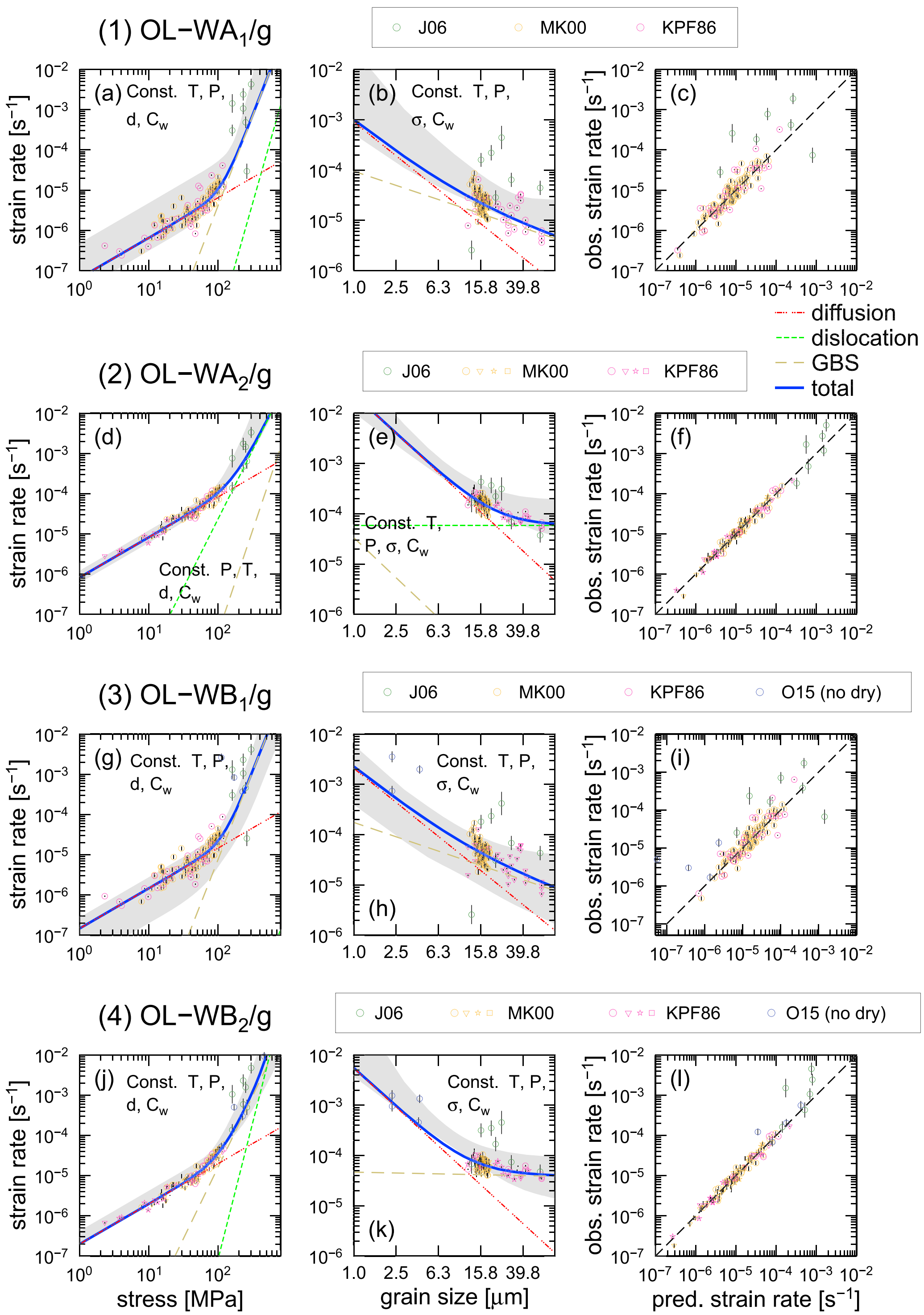

Figure 10. Same as Figure 8 but for the composite rheological model (II) (equation (13)). Here OL-WA$_1$/g and OL-WA$_2$/g represent our inversion results for global data set OL-WA with three inter-laboratory and nine interrun biases, respectively. OL-WB$_1$/g and OL-WB$_2$/g represent our results for global data set OL-WB with four inter-laboratory and 10 interrun biases, respectively (Table 3). Due to considerable nonuniqueness in the probability distributions for OL-WB$_2$/g, reported mean model is not a good fit to data. Well-fitting models can, however, be constructed for this case by perturbing the mean estimates within their 1σ bounds, taking correlations between parameters (Table S21) into account. The model predictions plotted here (j−l) correspond to a particular MCMC output that yielded a reasonably small misfit to data ($\chi^2_M/N \sim 128$). Contribution of grain boundary sliding (GBS) to the total strain rate is plotted as khaki dashed line in each panel. See also Figure S13.

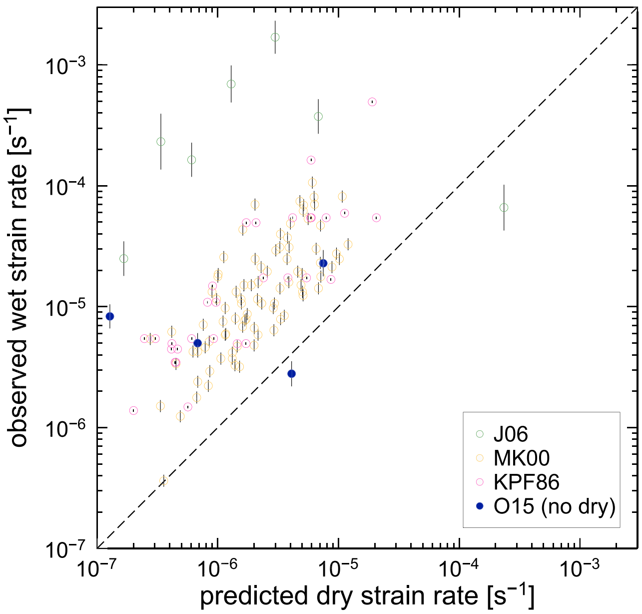

Figure 11. Comparison of strain rates observed under wet conditions with those predicted by a dry flow at corresponding experimental conditions. The dry flow law for OL-DB$_2$ is used to predict strain rates under dry conditions. Because the activation volumes V_1 and V_3 for the dry case are not estimated here, the values of V_2 and V_4, respectively, for model OL-WB$_1$ are used instead. Wet strain rates are corrected for interrun biases using the estimates on $X_1 - X_4$ for OL-WB$_1$. Error bars denote experimental uncertainties in strain rate.

Our results for models (I) and (II) (Tables 4 and 5) yield similar values of χ^2_{M}/N (e.g., Figures 7a and 9a), but the flow-law parameters for GBS are not uniquely resolved (Figures 9a and 9b). All our results are associated with large χ^2_{M} ($\chi^2_{\mathrm{M}}/N \gg 1$), suggesting that data uncertainties may have been underestimated. The uncertainty of stress could be larger than reported, particularly for high-pressure data. Stresses in J06 were derived from dislocation densities, and uncertainties associated with this estimation may be difficult to quantify accurately. In O15, stresses were measured at different crystallographic planes using X-ray diffraction, and their arithmetic average was assumed to represent the macroscopic stress. Such an assumption could introduce large errors in stress estimates, because the relation between microscopic and macroscopic stresses is not well understood (Karato, 2009).

4.2. Comparison With Previous Studies

Most of previous experimental studies, such as MK00a and Hirth and Kohlstedt (2003), have reported a grain-size exponent of 3 for diffusion creep, indicative of grain-boundary diffusion. Reanalysis of individual experimental runs of KPF86, MK00, and J06 has, however, revealed that single-run data of MK00a cannot constrain p_2 reliably (Jain et al., 2018). Our global inversions yield $p_2 \sim 2$, which suggests the dominance of bulk diffusion in olivine. MK00a is one of the few studies to have investigated the water-content exponent for diffusion creep. Constraints on r_2 returned by OL-WA$_1$ in our analysis partially overlap with the range 1.0 ± 0.3 suggested for r_2 by MK00a. OL-WA$_2$ yielded a lower estimate of ~ 0.3, which is also theoretically plausible. For the activation energy E_2, our estimates agree with 335 ± 75 kJ mol^{-1} suggested by Hirth and Kohlstedt (2003).

For dislocation creep, the stress exponent is constrained between 3.5 and 4 in this study, which is consistent with previous publications, such as Chopra and Paterson (1984), KPF86, Bai et al. (1991; single crystal data), and MK00b. Our estimates on the activation energy E_4 also overlap with published estimates, which vary between 410 ± 40 kJ mol^{-1} (Karato & Jung, 2003) and 480 ± 40 kJ mol^{-1} (e.g., MK00b; Hirth & Kohlstedt, 2003). The water-content exponent for dislocation creep is usually constrained at $\sim 1.2 \pm 0.4$ (e.g., MK00b, Karato & Jung, 2003), though a smaller value of $\sim$0.3 has been recently suggested (Fei et al., 2013). Our inversion results, however, indicate $r_4 > 2$.

Previous estimates on the activation volume for diffusion creep vary widely between 0 and 30 cm^3 mol^{-1} (Karato, 2010) because high-pressure data for this regime is lacking. Some studies, such as Karato and Jung (2003) and J06, have studied the effect of pressure on dislocation creep, but the range of pressures explored by these studies may still be too narrow, and the measurements too uncertain, to reliably constrain V_4 (e.g., Karato, 2010). Published estimates on V_4 range from 11 to 27 cm^3 mol^{-2}. If dislocation climb under wet conditions is rate limited by the diffusion of silicon ion in olivine, then V_4 as low as -2 cm^3 mol^{-1} may also be permitted (Bejina et al., 1997). Results of our global analyses, associated with large 1σ uncertainties, cannot resolve the ambiguity in V_2 and V_4. However, because more studies indicate positive values of V_i, our results for OL-WA$_1$, OL-WB$_1$, OL-WA$_1$/g, and OL-WB$_1$/g may be preferred over OL-WA$_2$, OL-WB$_2$, OL-WA$_2$/g, and OL-WB$_2$/g, respectively.

Not many experimental or theoretical studies have investigated deformation in olivine in the GBS regime under wet conditions. The inversion results of O15 for this mechanism are not entirely reproducible, indicating possible error in their analysis (see section S6). We thus cannot assess the consistency of our results with existing estimates on the flow-law parameters for GBS.

5. Discussion and Summary

5.1. Limitations of This Study

In this study, we conducted the global inversion of published experimental data on olivine aggregates, as the need of such global inversion had been suggested by the reanalysis of individual experimental runs

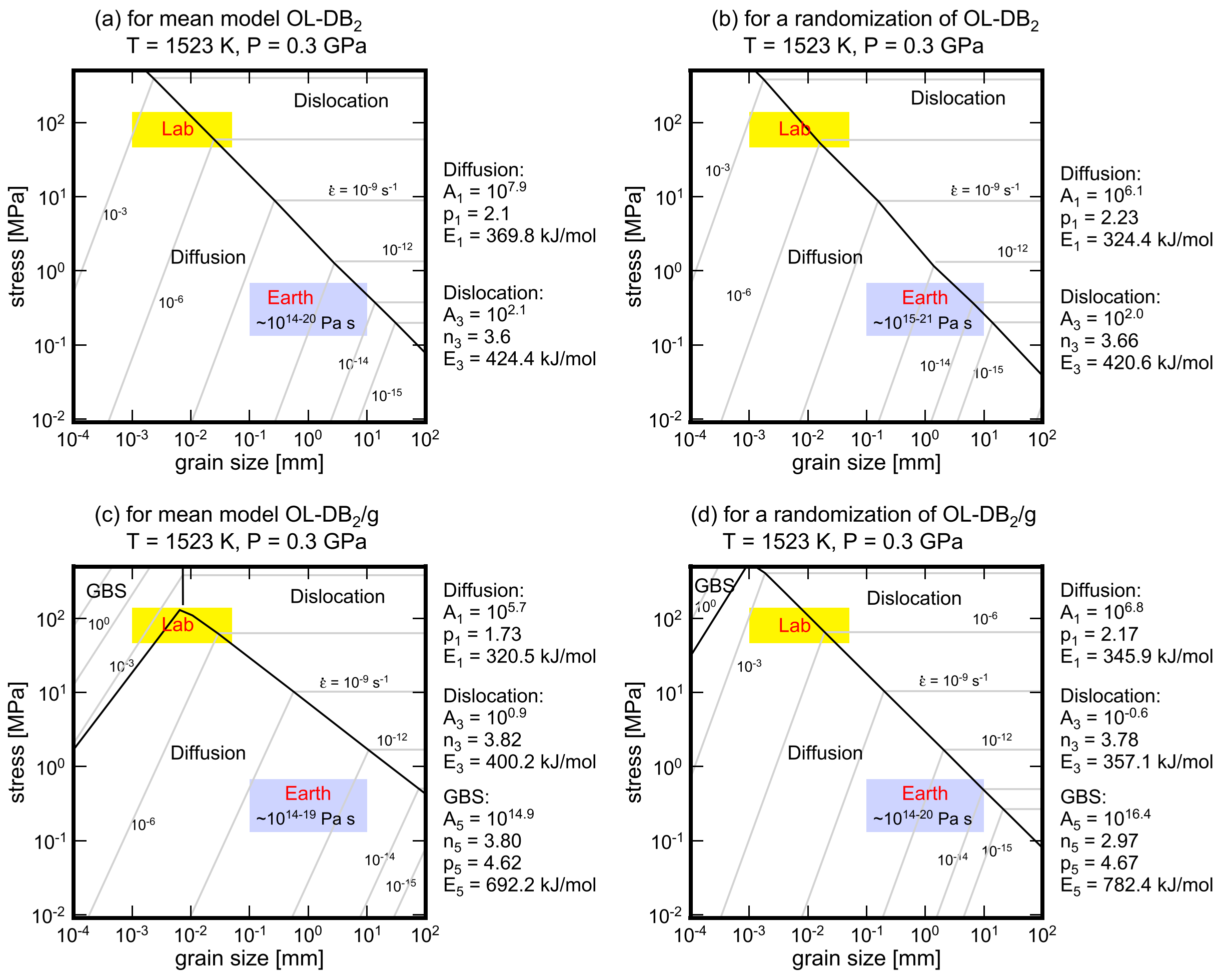

Figure 12. Deformation maps for dry olivine constructed using our Markov chain Monte Carlo inversion results for two different composite rheological models, one that assumes the parallel operation of diffusion and dislocation creep (a and b), represented by our model for case OL-DB$_2$, and another that also includes the contribution of grain boundary sliding (c and d), modeled by our case OL-DB$_2$/g. The temperature and pressure conditions for all maps are assumed to be 1,523 K and 0.3 GPa, respectively, relevant to a depth of ∼10 km in a warm lithosphere. Constant strain rate contours are drawn in grain size versus stress space. Maps (a) and (c) show predictions under these conditions made by the mean flow-law parameters for cases OL-DB$_2$ and OL-DB$_2$/g, respectively, whereas maps (b) and (d) are plotted using flow-law parameters obtained by randomizing the respective mean flow-law parameters for the two cases. The relevant flow-law parameters are mentioned alongside each panel. The range of grain sizes and stresses typical to deformation experiments conducted in laboratories (yellow rectangle) and those expected in the upper mantle (blue rectangle) are highlighted in each case. The box indicating conditions for Earth also indicates the effective viscosity predicted for the upper mantle by the corresponding flow laws.

(Jain et al., 2018). We also modified our MCMC inversion scheme to facilitate the handling of interrun bias in global inversion. For dry and wet conditions, we presented inversion results for four global data sets that differed either in size or the number of data groups considered. They were analyzed for two composite rheological models, that is, models (I) and (II). Our results indicate that considerable nonuniqueness exists in the flow-law parameters even with global inversion. This suggests that the data considered here are still insufficient. Large data uncertainties and incompatibility between data sets blur our constraints further.

As mentioned in section 2, we assumed that the water content of all wet samples is sufficiently high for the wet rheology to dominate. To verify the validity of this assumption, we compare our wet experimental data with the strain rates predicted by our dry flow law OL-DB$_2$ at the same temperatures, pressures, stresses, and grain sizes. Figure 11 shows that except for three data points, the strain rates observed under wet conditions are at least two times as fast as those predicted by the dry flow law, indicating that the contribution of the wet rheology is larger than that of the dry rheology in these data. Nevertheless, a number of these data may be deforming in the vicinity of the boundary between dry and wet rheologies. This boundary may be identified by analyzing all dry and wet data for a more comprehensive composite flow law that includes both dry and wet flow laws, but such an inversion would be difficult to conduct, given limited computational resources, and may not yield meaningful results with existing data, given their limitations.

The paucity of high-pressure data greatly affects our estimates on the effects of pressure. For dry conditions, only few high-pressure data are available. Global inversion with one such data set (Durham et al., 2009) is discussed in section S7. With only five data points provided by their study, resulting constraints on V_1 and V_3 are probably not robust. Our global data sets under wet conditions include more high-pressure data (Jung et al., 2006; Ohuchi et al., 2015), but their pressure range is still too narrow to reliably constrain the activation volumes. Because water fugacity depends strongly on pressure (Karato, 2008, chapter 2), our constraints on the water-content exponent may also be compromised. Tighter estimates on V_i and r_i should wait for more data at higher pressures (>6 GPa), such as those recently reported by Dixon and Durham (2018).

We also require data that finely sample the transition regime between diffusion and dislocation creep, to help resolve estimates on the flow-law parameters for GBS. The analysis of currently available data for model (II) suggests nontrivial contribution of GBS to the observed deformation. However, both models (I) and (II) yield similar fits to these data, meaning that the observed strain rates can be explained equally well with or without invoking GBS as a rate-limiting mechanism. Existing data are thus ambiguous about the significance of GBS in modeling olivine rheology.

Our results also indicate large interrun biases in our global data sets, especially under wet conditions, for example, the maximum value of $|X_m|$ is ~1 for dry data but ~5 for wet data. In future experimental studies, it will be important to minimize interrun biases because these errors also introduce some nonuniqueness in flow-law estimates. For example, we assume constant interrun bias for each data group, but in reality, it could vary gradually during an experiment ("drift condition"), such as due to gradual and unconstrained loss of water during an experiment. An incorrect assumption on the nature of interrun bias could yield erroneous estimates on flow-law parameters (section S8). However, a more involved treatment of interrun biases is difficult with the published information on experimental conditions. Recent studies have experimented with a new strategy in which deformation experiments are simultaneously conducted on multiple samples in the same assembly (e.g., Hansen et al., 2017; Katayama & Karato, 2008; Mohiuddin & Karato, 2018), which could drastically reduce interrun bias between data collected from different samples. Our MCMC inversion can quantify the efficacy of such a new approach.

5.2. On the Differences From KK08

One parameter that is nearly uniquely resolved in this study is the grain-size exponent for diffusion creep. It is constrained at ~2 in most of our models that exclude GBS, which indicates that diffusion creep occurs primarily by volumetric diffusion, in contrast to the conventional assumption of grain-boundary diffusion in olivine, and the geodynamic consequences of p_1 ~2 are briefly discussed in the next section. When our composite rheological model includes GBS, the sensitivity to grain size is distributed between diffusion creep and GBS, and the currently available data cannot uniquely resolve all flow-law parameters in this case. Nevertheless, all data sets included in our analysis constrain p_1 and p_2 well within the assumed a priori bounds and the theoretically permissible range of 1–3. This is in sharp contrast to the global inversion results of KK08, which indicated that the data sets OL-DA$_1$ and OL-WA$_1$ preferred values of p_1 and p_2 greater than 3 ["all dry" and "all wet" cases in Figures 6 and 11, respectively, of KK08]. The following reasons could explain the discrepancies between their results and ours.

First, the preference for $p_i \geq 3$ could be a result of parameter bias in their study. Second, they assumed narrow a priori bounds on all flow-law parameters and in particular used $2 \leq p_i \leq 3$. As discussed in section S1 of Jain et al. (2018), such restricted MCMC sampling can lead to an artificial peak in the a posteriori probability distributions at either end of the a priori range. Their choice of a priori bounds on X_m could similarly have influenced their inversion results. Third, unlike our study, KK08 had attempted to also estimate pressure effects under dry conditions. Because they analyzed only low-pressure data including the erroneous pressure-variable run PI-220 of MK00, the activation volumes could not be constrained. But correlation between V_i and p_1 could have prevented data from constraining p_1 within its a priori bounds, irrespective of the width of these bounds. Our results, on the other hand, are not affected by parameter bias (section 2.2), and we have assumed very wide a priori ranges in our study. Even though our choice of data grouping affects our results, the actual values of X_m do not, thanks to our "gradient fitting" approach (section 2.3). These arguments indicate that our results are more accurate than those of KK08.

5.3. Deformation Maps

The grain-size exponent of ∼2 for diffusion creep suggests that contrary to conventional expectations, Nabarro-Herring creep dominates in olivine under experimental conditions. Natural dunite samples contain much coarser grains that roughly range from 0.1 to 10 mm in size, as opposed to synthetic samples where grain sizes are usually on the order of a few microns. The assumption of a grain-size exponent of 2 instead of 3 could potentially lower our prediction for the upper mantle viscosity by 3 orders of magnitude. Typical stresses and strain rates expected in the upper mantle also differ from experimental conditions by many orders of magnitude. The revised flow-law parameters reported by us could, therefore, predict viscosities for the upper mantle that are much different from those expected from previously published flow laws. Geophysical techniques, such as postglacial rebound, constrain the upper mantle viscosity at $10^{19} - 10^{22}$ Pa s (e.g., Mitrovica & Forte, 2004), and predictions of conventionally assumed flow-law parameters, such as those reported by Hirth and Kohlstedt (2003) with $p_1 = 3$, are consistent with these geophysical estimates. It is thus important to verify the geophysical relevance of our inversion results. To this end, we plot deformation maps corresponding to the upper mantle conditions.

We present here four deformation maps for olivine under dry conditions and at 1,523 K and 0.3 GPa, which is representative of a depth of ∼10 km in the upper mantle. We cannot predict deformation at greater depths due to lack of constraints on the activation volumes. Whereas geological stresses, strain rates, and grain sizes at this depth are expected to be on the order of ∼1 MPa, $10^{-15} - 10^{-14}$ s^{-1}, and 1–10 mm, respectively, experimental conditions usually encompass stresses of 10–500 MPa and strain rates of 10^{-5} s^{-1} in 1- to 100-μm-sized grains, and we highlight both sets of conditions in our maps. Figure 12a shows a deformation map constructed using the mean flow-law parameters for the case OL-DB$_2$. This composite rheological model predicts that experimental conditions lie close to the boundary between diffusion and dislocation creep regimes, but the shallow upper mantle likely deforms entirely in the diffusion creep regime. The predictions of upper mantle viscosity are somewhat lower than expected.

Our MCMC inversion scheme enables us to evaluate the mean, the standard deviation, and correlation between various flow-law parameters, and using this information, we can randomize the mean model within its 1σ bounds to obtain another correlated set of flow-law parameters that are also consistent with the experimental data. We thus perturb the mean model for OL-DB$_2$ to obtain a correlated set of flow-law parameters. The deformation map constructed using this perturbed flow law (Figure 12b) predicts upper mantle viscosities that overlap with the geophysical estimates. Moreover, the deformation map suggests that conditions in the upper mantle lie in the transition regime between diffusion and dislocation creep, which is consistent with the observations of anisotropy in the shallow mantle (e.g., Hirth & Kohlstedt, 2003; Karato & Wu, 1993; Skemer et al., 2010). We may then infer that some randomizations of our mean flow law for case OL-DB$_2$ could be consistent with geophysical observations.

Similarly, Figures 12c and 12d present deformation maps for the case OL-DB$_2$/g, where GBS is also considered to be a rate-limiting mechanism. The corresponding mean flow law and one of its randomizations predict lower than expected viscosities for the upper mantle. Moreover, diffusion creep is expected to dominate under the shallow upper mantle conditions if the mean flow law is considered (Figure 12c). For the randomized flow law, the dominant deformation mechanism would transition from diffusion to dislocation creep at coarser grain sizes of ∼20 mm. The GBS regime does not appear to play any role in upper mantle rheology for both flow laws even though laboratory conditions in Figure 12c lie in the transition region between diffusion creep, dislocation creep, and GBS.

5.4. Conclusions

In this study, we presented 16 possible composite flow laws that can fit experimental data well. Some of our results may not be theoretically acceptable (sections 3.3 and 4.2), for example, OL-DA$_2$, OL-DA$_1$/g, OL-DA$_2$/g, and OL-DB$_1$/g (under dry conditions) and OL-WA$_2$, OL-WB$_2$, OL-WA$_2$/g, and OL-WB$_2$/g (under wet conditions). The remaining cases, that is, OL-DA$_1$, OL-DB$_1$, OL-DB$_2$, and OL-DB$_2$/g (under dry conditions) and OL-WA$_1$, OL-WB$_1$, OL-WA$_1$/g, and OL-WB$_1$/g (under wet conditions), serve as candidate flow laws to model olivine rheology.

The candidate flow laws reported here are more useful for application in geodynamic studies than previously published flow laws, for the following reasons. First, we report composite flow laws, which are more realistic models for deformation under both laboratory and mantle conditions. Analyzing data simultaneously for more than one creep mechanism also yields a self-consistent composite flow law. Furthermore, as our inversion results agree with experimental data from multiple studies, they are more reliable. The a posteriori probability distributions of model parameters provided by MCMC inversion also allow us to gauge the quality of experimental constraints.

We can also determine correlation between various model parameters using our MCMC output (Tables S2–S5, S7–S10, S13–S16, and S18–S21). Knowing the mean and standard deviation for each flow-law parameter, and the correlation between parameters, we can compute confidence intervals about our mean predictions to quantify their reliability (e.g., the prediction of mantle viscosities by KK08). Such statistical assessment cannot be done with most of previously published flow-law parameters because covariance among parameters belonging to different deformation mechanisms has not been assessed in most of these studies. Our global analysis, based on MCMC inversion, therefore, provides the means to not only derive constraints on rock mechanics but also assess the reliability of these constraints for geodynamical applications.

Appendix A: How to Determine Scaling Constants

To explain our modification to the conjugate gradient algorithm of Mullet et al. (2015), we rewrite our model equation (8) as follows:

$$\begin{aligned}\dot{\epsilon}_{obs,a} &= \left(A_1 f_1\left(\{q_k\};\{s_l^a\}\right) + A_2 f_2\left(\{q_k\};\{s_l^a\}\right) + \ldots\right)\cdot \exp(X_m)\\ &= A_1\left(f_1\left(\{q_k\};\{s_l^a\}\right) + \frac{A_2}{A_1} f_2\left(\{q_k\};\{s_l^a\}\right) + \ldots\right)\cdot\exp(X_m)\\ &= A_1\left(\sum_{i=1}^{n_i} B_i f_i\left(\{q_k\};\{s_l^a\}\right)\right)\cdot\exp(X_m),\end{aligned} \tag{A1}$$

where $f_i\left(\{q_k\};\{s_l^a\}\right) = \dot{\epsilon}_i\left(\{q_k\};\{s_l^a\}\right)/A_i$ for the ith flow law at the ath data point of the mth group, $B_i = A_i/A_1$, and our composite rheological model assumes the parallel operation of n_i mechanisms. If $\Delta_{a,b}^m$ (equation (10)) is evaluated with this version of the model equation instead of equation (8), we can eliminate both A_1 and X_m from the misfit function χ_J^2 (equation (11)). In order to minimize χ_J^2, therefore, we need to determine the values of B_i for $i > 1$ that best fit the gradient between all data pairs within a group and for all data groups. Consequently, we use the conjugate gradient method to estimate the best possible values of B_i for $i > 1$ instead of A_i. Once B_i is evaluated, and A_1 is known, we can easily derive each A_i for $i > 1$ from B_i.

The estimation of A_1 is, however, coupled with that of X_m. We can substitute the values of B_i returned by the conjugate gradient method in equation (A1) to estimate $A_m^X = A_1 \cdot \exp(X_m)$ for each data group using linear regression. If our data set contains M groups, we will obtain M values of A_m^X. The value of A_1, however, must be identical for all data, but X_m is assumed to be identical only for data within the same group. The average of the M estimates on $\log A_m^X$, denoted by $\overline{\log A^X}$, is then assigned to $\log A_1$, and $X_m = \overline{\log A^X} - \log A_m^X$ for $m = 1, \ldots, M$.

Appendix B: Distribution of Errors in Strain Rate

All experimental observations are associated with some uncertainty due to the limited resolution of a measuring instrument. These uncertainties are usually assumed to be normally distributed. Uncertainty associated with strain rate originates from the uncertainty, δL, in the measurements of original length, L_0, of the sample and the length after deformation, L_1. Errors in L_0 and L_1 may, therefore, be normally distributed, but the value of the resulting strain, calculated as $\left(1 - L_1/L_0\right)$, would follow a ratio distribution, defined as the ratio of two distributions. The uncertainty of strain is, however, reported as $\delta L/L_0$ and assumed to be normally distributed, which is a reasonable approximation considering that δL is usually quite small. Below, we justify our assumption that the distribution of errors in the logarithm of strain too can be approximated by a Gaussian distribution.

Here we consider a concrete example, but the nature of our conclusion is quite general. Let L_0 be 100 μm, and δL be 2 μm. Reported uncertainty in the measurements of strain ($\delta\epsilon$) would, therefore, be of $\delta L/L_0 = 0.02$. Let us further assume that L_1 is 80 μm. Expected strain in the sample (ϵ_0) is, therefore, 0.2 (positive for compression). This value is associated with $\delta\epsilon = 0.02$, which is 10 % of the observed (expected) value of ϵ_0. Uncertainty in the logarithm of strain [$\delta(\log\epsilon)$] is, therefore, also $0.02/0.2 = 0.1$ or 10%.

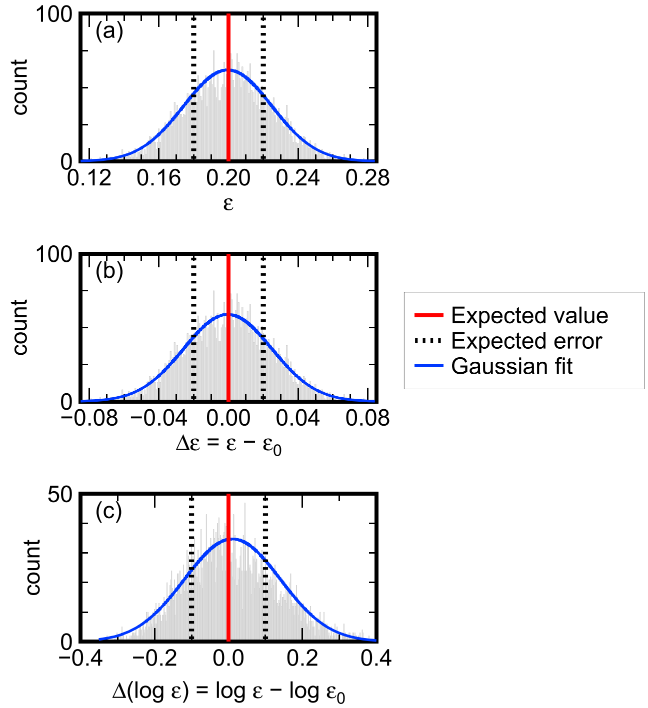

Figure B1. Understanding the distribution of errors associated with the measurement of strain for a reported uncertainty of 10%. Histograms represent distribution of (a) observations of strain, ϵ, about their expected value $\epsilon_0 = 0.2$ (red solid), when reported uncertainty in σ_0 is 0.02 (black dotted); (b) the deviation, $\Delta\epsilon$, of the observed strain from its expected value of ϵ_0, and (c) the deviation of $\log(\epsilon)$ from $\log(\epsilon_0)$, where the expected uncertainty in the measurement of $\log(\epsilon_0)$ is 0.10 (black dotted). Also shown is a Gaussian curve (blue) that is fit to each distribution.

However, actual error in the observed strain are associated with the measurement of L_0 and L_1, as mentioned earlier. We, therefore, study the distribution of errors by randomizing L_0 and L_1 with $\pm$ 2 μm, assuming that errors in length are normally distributed and generate 5,000 possible realizations of strain (ϵ). Figure B1a confirms that our synthetic values of ϵ are indeed normally distributed about a mean value that coincides with the expected value $\epsilon_0 = 0.2$. The deviation of ϵ from its expected value, $\Delta\epsilon = \epsilon - \epsilon_0$, is, therefore, also normally distributed (Figure B1b) with one standard deviation of ∼0.02.

Figure B1c indicates that the deviation of the logarithm of strain from its expected value, $\Delta(\log \epsilon) = \log \epsilon - \log \epsilon_0$, can also be approximated by a normal distribution with one standard deviation of ∼0.1, equivalent to the expected log error of 10 %. Similar analysis with larger uncertainty yields that the distribution of $\Delta(\log \epsilon)$ starts to deviate from a gaussian prediction for $\delta\epsilon > 10$ %. This suggests that if strain is associated with up to 10 % uncertainty, then the uncertainty in its logarithm can be assumed to be normally distributed. This analysis is extended to strain rates under the assumption of negligible error in the measurement of time. Because only a few data points in our global compilation are associated with such larger than 10% uncertainty in strain rates, our assumption that errors in $\log(\dot{\epsilon})$ are normally distributed is deemed acceptable.

Acknowledgments
This work was sponsored by the U.S. National Science Foundation under grant OCE-1417327. This work was also supported in part by the facilities and staff of the Yale University Faculty of Arts and Sciences High Performance Computing Center. Reviews by Lars Hansen and an anonymous reviewer were helpful to improve the manuscript. All of experimental data analyzed in this study are available in Karato et al. (1986), Hirth and Kohlstedt (1995), and Mei and Kohlstedt (2000a, 2000b), Jung et al. (2006), Hansen et al. (2011), and Ohuchi et al. (2015), and data uncertainties are tabulated in our study.

References

Alisic, L., Gurnis, M., Stadler, G., Burstedde, C., & Ghattas, O. (2012). Multi-scale dynamics and rheology of mantle flow with plates. *Journal of Geophysical Research*, *117*, B10402. https://doi.org/10.1029/2012JB009234

Bai, Q., Mackwell, S. J., & Kohlstedt, D. L. (1991). High-temperature creep of olivine single crystals, 1. Mechanical results for buffered samples. *Journal of Geophysical Research*, *96*, 2441–2463.

Bejina, F., Raterron, P., Zhang, J., Jaoul, O., & Lierbermann, R. C. (1997). Activation volume of silicon diffusion in san carlos olivine. *Geophysical Research Letters*, *24*, 2597–2600.

Carter, N. L., & Ave'Lallemant, H. G. (1970). High temperature flow of dunite and peridotite. *Geological Society of America Bulletin*, *81*, 2181–2202.

Chopra, P. N., & Paterson, M. S. (1984). The role of water in the deformation of dunite. *Journal of Geophysical Research*, *89*, 7861–7876.

Dixon, N. A., & Durham, W. B. (2018). Measurement of activation volume for creep of dry olivine at upper-mantle conditions. *Journal of Geophysical Research: Solid Earth*, *123*, 8459–8473. https://doi.org/10.1029/2018JB015853

Durham, W. B., Mei, S., Kohlstedt, D. L., Wang, L., & Dixon, N. A. (2009). New measurements of activation volume in olivine under anhydrous conditions. *Physics of the Earth and Planetary Interiors*, *172*, 67–73.

Faul, U. H., Fitz Gerald, J. D., Farla, R. J. M., Ahlefeldt, R., & Jackson, I. (2011). Dislocation creep of fine-grained olivine. *Journal of Geophysical Research*, *116*, B01203. https://doi.org/10.1029/2009JB007174

Faul, U. H., & Jackson, I. (2007). Diffusion creep of dry, melt-free olivine. *Journal of Geophysical Research*, *112*, B04204. https://doi.org/10.1029/2006JB004586

Fei, H., Wiedenbeck, M., Yamazaki, D., & Katsura, T. (2013). Small effect of water on upper-mantle rheology based on silicon self-diffusion coefficients. *Nature*, *498*, 213–215.

Garel, F., Goes, S., Davies, D. R., Davies, J. H., Kramer, S. C., & Wilson, C. R. (2014). Interaction of subducted slabs with the mantle transition-zone: A regime diagram from 2-D thermo-mechanical models with a mobile trench and an overriding plate. *Geochemistry, Geophysics, Geosystems*, *15*, 1739–1765. https://doi.org/10.1002/2014GC005257

Hansen, L. N., Kumamoto, K. M., Thom, C., Wallis, D., Goldsby, D. L., Durham, W. B., & Kohlstedt, D. L. (2017, December). *The grain-size dependence of yield strength during low-temperature plasticity of olivine: Evidence for weak lithospheric mantle*. In AGU Fall Meeting Abstracts.

Hansen, L. N., Zimmerman, M. E., & Kohlstedt, D. L. (2011). Grain boundary sliding in San Carlos olivine: Flow law parameters and crystallographic-preferred orientation. *Journal of Geophysical Research*, *116*, B08201. https://doi.org/10.1029/2011JB008220

Hedjazian, N., Garel, F., Davies, D. R., & Kaminski, E. (2017). Age-independent seismic anisotropy under oceanic plates explained by strain history in the asthenosphere. *Earth and Planetary Science Letters*, *460*, 135–142.

Hirth, G., & Kohlstedt, D. L. (1995). Experimental constraints on the dynamics of the partially molten upper mantle: Deformation in the diffusion creep regime. *Journal of Geophysical Research*, *100*, 1981–2001.

Hirth, G., & Kohlstedt, D. L. (2003). Rheology of the upper mantle and the mantle wedge: A view from the experimentalists. In J. Eiler (Ed.), *Inside the subduction factory* (pp. 83–105). Washington, D.C: AGU.

Hirth, G., & Kohlstedt, D. L. (2015). The stress dependence of olivine creep rate: Implications for extrapolation of lab data and interpretation of recrystallized grain size. *Earth and Planetary Science Letters*, *418*, 20–26.

Jain, C., Korenaga, J., & Karato, S.-I. (2018). On the grain size sensitivity of olivine rheology. *Journal of Geophysical Research: Solid Earth*, *123*, 674–688. https://doi.org/10.1002/2017JB014847

Jung, H., Katayama, I., Jiang, Z., Hiraga, T., & Karato, S.-I. (2006). Effect of water and stress on the lattice-preferred orientation of olivine. *Tectonophysics*, *421*, 1–22.

Karato, S.-I. (1989). Grain growth kinetics in olivine aggregates. *Tectonophysics*, *168*, 255–273.

Karato, S.-I. (2008). *Deformation of earth materials: Introduction to the rheology of the solid earth*. New York: Cambridge University Press.

Karato, S.-I. (2009). Theory of lattice strain in a material undergoing plastic deformation: Basic formulation and applications to a cubic crystal. *Physical Review B*, *79*(21), 214106. https://doi.org/10.1103/PhysRevB.79.214106

Karato, S.-I. (2010). Rheology of the deep upper mantle and its implications for the preservation of the continental roots. *Tectonophysics*, *481*, 82–98. https://doi.org/10.1016/j.tecto.2009.04.011

Karato, S.-I., & Jung, H. (2003). Effects of pressure on high-temperature dislocation creep in olivine. *Philosophical Magazine*, *83*, 401–414.

Karato, S.-I., Paterson, M., & Fitzgerald, J. D. (1986). Rheology of synthetic olivine aggregates: Influence of grain size and water. *Journal of Geophysical Research*, *91*, 8151–8176.

Karato, S.-I., & Wu, P. (1993). Rheology of the upper mantle: A synthesis. *Science*, *260*, 771–778.

Katayama, I., & Karato, S.-I. (2008). Effects of water and iron content on the rheological contrast between garnet and olivine. *Physics of the Earth and Planetary Interiors*, *166*(1-2), 57–66.

Kohlstedt, D. L., Evans, B., & Mackwell, S. J. (1995). Strength of the lithosphere: Constraints imposed by laboratory experiments. *Journal of Geophysical Research*, *100*, 17,587–17,602.

Kohlstedt, D. L., Keppler, H., & Rubie, D. C. (1996). Solubility of water in the α, β and γ phases of $(Mg,Fe)_2SiO_4$. *Contributions to Mineralogy and Petrology*, *123*, 345–357.

Korenaga, J., & Karato, S.-I. (2008). A new analysis of experimental data on olivine rheology. *Journal of Geophysical Research*, *113*, B02403. https://doi.org/10.1029/2007JB005100

Langdon, T. G. (1994). Unified approach to grain boundary sliding in creep and superplasticity. *Acta Metallurgica et Materialia*, *42*, 2437–2443. https://doi.org/10.1016/0956-7151(94)90322-0

Langdon, T. G. (2006). Grain boundary sliding revisited: Developments in sliding over four decades. *Journal of Materials Science*, *41*(3), 597–609. https://doi.org/10.1007/s10853-006-6476-0

Langdon, T. G. (2009). Seventy-five years of superplasticity: Historic developments and new opportunities. *Journal of Materials Science*, *44*(22), 5998–6010. https://doi.org/10.1007/s10853-009-3780-5

Mei, S., & Kohlstedt, D. L. (2000a). Influence of water on plastic deformation of olivine aggregates, 1. Diffusion creep regime. *Journal of Geophysical Research*, *105*, 21,457–21,469.

Mei, S., & Kohlstedt, D. L. (2000b). Influence of water on plastic deformation of olivine aggregates, 2, Dislocation creep regime. *Journal of Geophysical Research*, *105*, 21471–21481.

Mitrovica, J. X., & Forte, A. M. (2004). A new inference of mantle viscosity based upon joint inversion of convection and glacial isostatic adjustment data. *Earth and Planetary Science Letters*, *225*, 177–189.

Mohiuddin, A., & Karato, S.-I. (2018, April). *Influence of olivine to wadsleyite/ringwoodite phase transformation on the rheology of the transition zone*. In 20th EGU General Assembly Conference Abstracts (Vol. 20, p. 3678).

Mullet, B. G., Korenaga, J., & Karato, S.-I. (2015). Markov chain Monte Carlo inversion for the rheology of olivine single crystals. *Journal of Geophysical Research: Solid Earth*, *120*, 3142–3172. https://doi.org/10.1002/2014JB011845

Ohuchi, T., Kawazoe, T., Higo, Y., Funakoshi, K. I., Suzuki, A., Kikegawa, T., & Irifune, T. (2015). Dislocation-accommodated grain boundary sliding as the major deformation mechanism of olivine in the Earth's upper mantle. *Science Advances*, *1*, E1500360. https://doi.org/10.1126/sciadv.1500360

Poirier, J.-P. (1985). *Creep of crystals: High-temperature deformation processes in metals, ceramics and minerals*. Cambridge and New York: Cambridge University Press.

Skemer, P., Warren, J. M., Kelemen, P. B., & Hirth, G. (2010). Microstructural and rheological evolution of a mantle shear zone. *Journal of Petrology*, *51*, 43–53.

Solomatov, V. S. (1995). Scaling of temperature and stress dependent viscosity convection. *Physics of Fluids*, *7*, 266. https://doi.org/10.1063/1.868624

Zhao, Y.-H., Ginsberg, S. B., & Kohlstedt, D. L. (2004). Solubility of hydrogen in olivine: Dependence on temperature and iron content. *Contributions to Mineralogy and Petrology*, *147*, 155–161.